Multilevel variational spectroscopy using a programmable quantum simulator

Zhikun Han,[1,2,3,*] Chufan Lyu,[4,*] Yuxuan Zhou,[1,2,3,5,*] Jiahao Yuan,[1,2,3,5] Ji Chu,[1,2,3] Wuerkaixi Nuerbolati,[1,2,3] Hao Jia,[1,2,3] Lifu Nie,[1,2,3] Weiwei Wei,[1,2,3] Zusheng Yang,[1,2,3] Libo Zhang,[1,2,3] Ziyan Zhang,[1,2,3] Chang-Kang Hu,[1,2,3] Ling Hu,[1,2,3] Jian Li,[1,2,3] Dian Tan,[1,2,3] Abolfazl Bayat,[4,6,†] Song Liu,[1,2,3,‡] Fei Yan ⓞ,[1,2,3,§] and Dapeng Yu[1,2,3,5,‖]

[1]*Shenzhen Institute for Quantum Science and Engineering, Southern University of Science and Technology, Shenzhen, Guangdong, China*
[2]*International Quantum Academy, Shenzhen, Guangdong, China*
[3]*Guangdong Provincial Key Laboratory of Quantum Science and Engineering, Southern University of Science and Technology, Shenzhen, Guangdong, China*
[4]*Institute of Fundamental and Frontier Sciences, University of Electronic Science and Technology of China, Chengdu, China*
[5]*Department of Physics, Southern University of Science and Technology, Shenzhen, Guangdong, China*
[6]*Key Laboratory of Quantum Physics and Photonic Quantum Information, Ministry of Education, University of Electronic Science and Technology of China, Chengdu, China*

Energy spectroscopy is a powerful tool with diverse applications across various disciplines. Variational quantum-classical algorithms based on programmable digital quantum simulators have emerged as promising approaches for conducting spectroscopy on various models using a single device, despite facing significant quantum and classical resource overheads. Here, we experimentally demonstrate multilevel variational spectroscopy for fundamental many-body Hamiltonians using a superconducting digital quantum simulator. By exploiting symmetries and the subspace search method, we achieve full spectroscopy for a four-qubit Heisenberg spin chain, yielding an average energy deviation as small as 0.13 from the theoretical values, assuming unity coupling strength. Our method, when extended to eight-qubit Heisenberg and transverse-field Ising Hamiltonians, successfully determines the three lowest-energy levels. In achieving the above, we introduce a circuit-agnostic compilation method that enhances the robustness of our simulator against signal crosstalk. Our study highlights the combination of the subspace search method and symmetry-assisted resource efficiency in variational quantum algorithms and lays the foundation for practical spectroscopy on near-term quantum simulators, with potential applications in quantum chemistry and condensed matter physics.

I. INTRODUCTION

Energy spectrum is a unique fingerprint of matter which makes spectroscopy [1–4] an indispensable tool in a range of scientific fields, including exoplanet composition determination, climate monitoring, and material synthesis. Recent advances in quantum simulation have lead to the emergence of analog and digital quantum simulators implemented on various physical platforms, such as cold atoms [5], ion-traps [6,7], nuclear magnetic resonance systems [8], photonic chips [9–11], Rydberg atoms [12], and superconducting circuits [13–20]. Although analog quantum simulators have been employed for spectroscopy by means of Fourier transform in a single-excitation manifold [21], their scalability and applicability to arbitrary Hamiltonians remain limited.

Digital quantum simulators, based on programmable quantum circuits, provide remarkable versatility and enable the study of arbitrary Hamiltonians [22]. Variational quantum algorithms, such as the variational quantum eigensolver (VQE) [23], present a promising avenue for exploring practical quantum applications using near-term quantum simulators. By employing a hybrid approach that combines a quantum simulator with a classical optimizer, VQE simulations have successfully tackled ground-state problems of many-body systems in quantum chemistry [24–29] and condensed matter physics [30,31]. However, the considerable resource overheads associated with both quantum and classical components have restricted VQE spectroscopy for predominantly targeting limited eigenstates in small system sizes [28,32–36]. To make quantum variational spectroscopy extensible, it is crucial to address resource overheads by simplifying the ansatz and reducing variational parameters. In fact, symmetry is a fundamental property that is found in every building block of our universe. The interaction between particles in strongly correlated many-body systems reveals several forms of symmetries. Several theoretical [37–40] and experimental [30,35,36] works tried to exploit such symmetries for either reducing quantum and classical resources in a VQE algorithm

*These authors have contributed equally to this work.

†abolfazl.bayat@uestc.edu.cn

‡lius3@sustech.edu.cn

§yanfei@baqis.ac.cn; Present address: Beijing Academy of Quantum Information Sciences, Beijing, China.

‖yudp@sustech.edu.cn

or targeting multiple eigenstates. However, relying on symmetries alone is not sufficient to simulate those eigenstates that share the same symmetries. An alternative way to simulate multiple eigenstates is the subspace search VQE (SSVQE) method [41] in which a quantum circuit is trained to simulate several eigenstates using multiple orthogonal initial states. By increasing the number of target eigenstates the SSVQE becomes highly resource demanding [38], which makes its experimental realization challenging and limited to small system sizes [42]. Indeed, to make multilevel variational quantum spectroscopy truly successful, one not only needs to combine these techniques, but also to exploit error mitigation techniques in both hardware and data processing levels, all adding to the experimental complexity.

In this article, we present an experimental demonstration of multilevel energy spectroscopy for fundamental many-body Hamiltonians using VQE on a superconducting digital quantum simulator. By employing a mix of symmetry-preserving ansatzes, we significantly reduce circuit depth and the number of variational parameters while targeting multiple energy levels in conjunction with the SSVQE method [41]. We also introduce a circuit compiling method that conveniently corrects for both spatial and temporal signal crosstalk, improving the consistency of the gate performance in our device. All these techniques are combined with error mitigation to enhance the accuracy of our method. We achieve full variational quantum spectroscopy for all 16 states of a four-qubit Heisenberg spin chain, with the measured energies deviating from their theoretical values by 0.13, on average, assuming a unity coupling strength. We further extend our approach to eight-qubit Heisenberg and transverse-field Ising Hamiltonians, extracting the three lowest-energy eigenstates and demonstrating the potential of our method for multilevel spectroscopy in many-body systems. Intriguingly, we find that, in the cases where the cost function of the VQE algorithm contains several terms, the best convergence result is obtained using a hybrid optimizer that combines the gradient-free Nelder-Mead method with the gradient-based Adam method.

II. SUBSPACE SEARCH VARIATIONAL QUANTUM EIGENSOLVER

As illustrated in Fig. 1(a), the VQE algorithm contains a quantum hardware unit that executes a quantum circuit consisting of an initialization part, a multilayer parameterized circuit, and measurement. The initialization circuit prepares an initial state of an N-qubit system through unitary operation $|\Phi\rangle = U_I|0\rangle^{\otimes N}$. The parameterized circuit, however, is described by a unitary operation $U(\vec{\theta})$, where $\vec{\theta} = (\theta_1, \theta_2, \ldots, \theta_l)$ are variational parameters. The action of $U(\vec{\theta})$ on the initial state creates the output state $|\Psi(\vec{\theta})\rangle = U(\vec{\theta})|\Phi\rangle$ for which an observable can be efficiently measured. A proper cost function $C(\vec{\theta})$ is calculated from the measured data, which is then fed into a classical optimizer to be minimized through updating the circuit parameters $\vec{\theta}$, a training process until an optimal set of parameters $\vec{\theta}^*$ is obtained.

In comparison to typical VQE algorithms, which find the ground state of a given Hamiltonian with the cost function being its expectation value [23–27,30,43], we employ

a combination of several techniques to extend the spectrum and target more excited states. For a system with known symmetries, we can prepare an initial state with a specific set of symmetry numbers and then apply the corresponding symmetry-preserving circuit such that the search is restricted within a certain manifold. In this way, one can easily obtain the lowest-energy eigenstate in that manifold, but an excited state to the whole system. For cases when the states are indistinguishable by symmetry or when it is hard to prepare the initial state, simulating the excited states requires either adding additional penalizing terms in the cost function [34,44] or simultaneous learning of multiple eigenstates through special training methods, such as SSVQE [41]. In our experiment, we use a general form for the cost function

$$C(\vec{\theta}) = \sum_{i=1}^{P} w_i \langle \Phi_i | U^\dagger(\vec{\theta}) H U(\vec{\theta}) | \Phi_i \rangle, \tag{1}$$

where $\{|\Phi_i\rangle\}_{i=1}^{P}$ are a set of P orthogonal initial states and w_i (real positive) are their weights with condition $w_1 > w_2 > \cdots > w_P$. Note that the output states $|\Psi_i\rangle = U(\vec{\theta})|\Phi_i\rangle$ are naturally orthogonal due to the unitarity of $U(\vec{\theta})$. With proper constraints imposed on these weights, one obtains $|E_i\rangle \approx |\Psi_i(\vec{\theta}^*)\rangle$ through classical minimization of the cost function, provided that the parameterized circuit exhibits adequate expressibility. Parallel algorithms have also been developed to accelerate both the VQE [45] and even the SSVQE algorithms [46].

III. EXPLOITING SYMMETRIES

To understand how symmetry is integrated into the algorithm, let us first examine the well-known Heisenberg spin-chain model that contains N spin-1/2 particles. The Hamiltonian is expressed by

$$H = J \sum_{i=1}^{N-1} \boldsymbol{\sigma}^i \cdot \boldsymbol{\sigma}^{i+1}, \tag{2}$$

where $J > 0$ is the coupling strength and $\boldsymbol{\sigma}^i = (\sigma_x^i, \sigma_y^i, \sigma_z^i)$ is the vector of Pauli operators at site i. The Heisenberg Hamiltonian in Eq. (2) supports several symmetries including (i) the magnetization in every direction, i.e., $[H, S_\alpha] = 0$, where $S_\alpha = \frac{1}{2} \sum_i \sigma_\alpha^i$ with $\alpha = x, y, z$; (ii) the total spin, i.e., $[H, S_{\text{tot}}^2] = 0$, where $S_{\text{tot}}^2 = S_x^2 + S_y^2 + S_z^2$; (iii) mirror symmetry, i.e., $[H, \mathcal{M}] = 0$, where the mirror operator $\mathcal{M}$ is defined as $\mathcal{M}|b_1 b_2 \ldots b_N\rangle = |b_N \ldots b_2 b_1\rangle$ with $|b_i\rangle = |0\rangle$ or $|1\rangle$ is the qubit state at site i. These symmetries imply that all the eigenstates $|E_j\rangle$ have a specific total spin s, namely, $S_{\text{tot}}^2|E_j\rangle = s(s+1)|E_j\rangle$, z-magnetization s_z, given by $S_z|E_j\rangle = s_z|E_j\rangle$ in which $-s \leqslant s_z \leqslant s$, and the mirror symmetry $m = \pm 1$, given by $\mathcal{M}|E_j\rangle = m|E_j\rangle$.

In general, each layer of our parameterized circuit contains two consecutive sets of two-qubit operations $\mathcal{N}(\theta)$, acting on odd and even bonds, followed by a series of single-qubit rotations [see Fig. 1(a)]. In the case of the Heisenberg model, $\mathcal{N}(\theta)$ acting on qubits i and $i+1$ is chosen to be

$$\mathcal{N}_H(\theta) = e^{i\theta\left(\sigma_x^i \sigma_x^{i+1} + \sigma_y^i \sigma_y^{i+1} + \sigma_z^i \sigma_z^{i+1}\right)}. \tag{3}$$
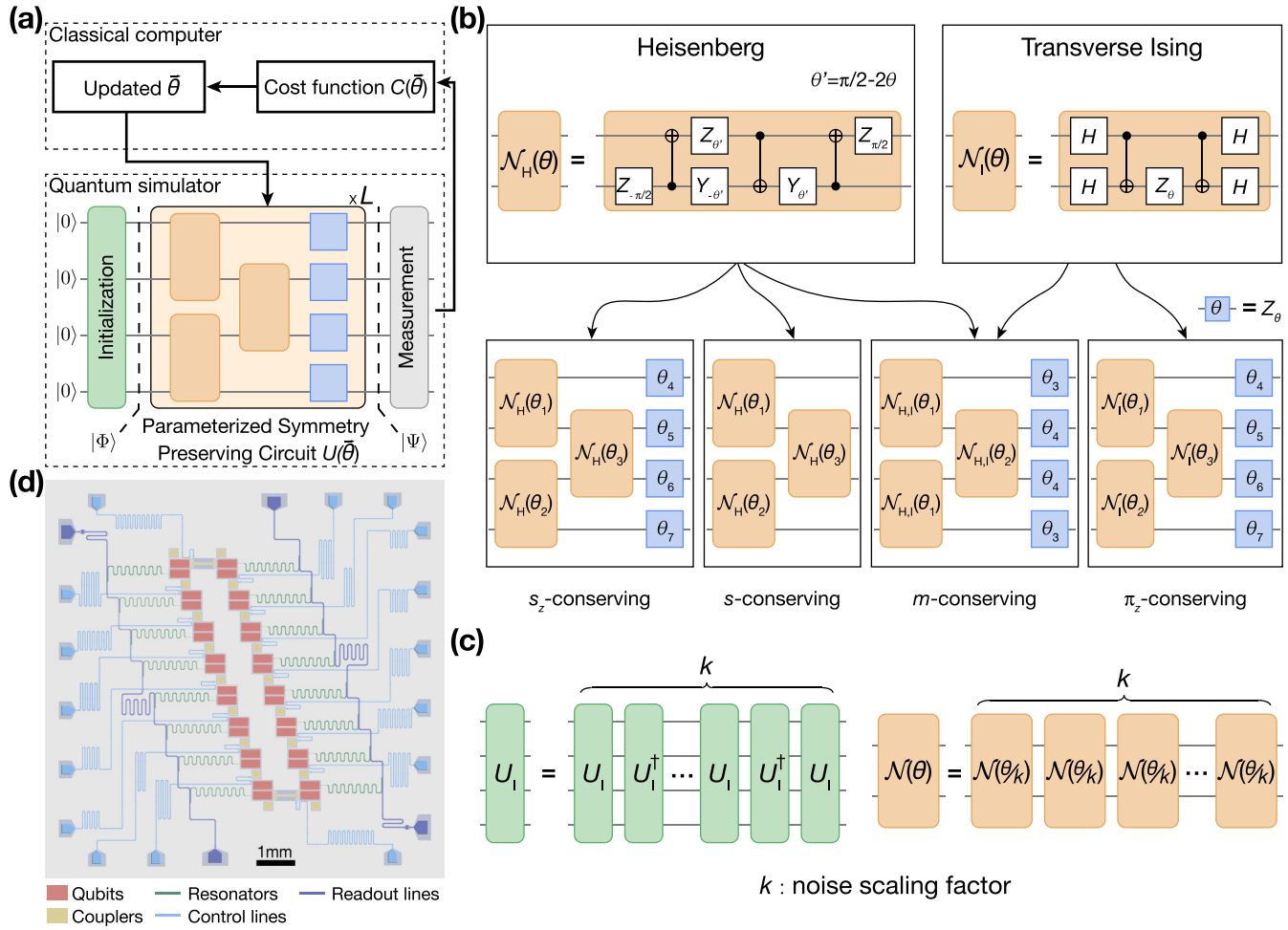
FIG. 1. Variational quantum algorithm with symmetry-preserving circuits. (a) Schematic diagram of a variational quantum algorithm which is realized on a combination of a quantum simulator and a classical computer. The quantum circuit includes an initialization circuit U_I, a parameterized symmetry-preserving circuit $U(\vec{\theta})$, and a measurement unit. The measurement results are fed into a classical optimizer for minimizing a cost function $C(\vec{\theta})$ through iteratively updating the parameters $\vec{\theta}$. (b) Ansatz circuits for preserving different symmetries. In the top boxes are the two-qubit modular circuits used for the Heisenberg and transverse-field Ising problems. In the bottom are ansatz circuits for preserving z-polarization (s_z), total spin (s), mirror symmetry (m), and zz-product (π_z), respectively. (c) Error mitigation using zero-noise extrapolation. U_I and $U_I^\dagger$ are the initialization circuit and its reversal. Note that the $\mathcal{N}(\theta/k)$ circuit is identical to the original $\mathcal{N}(\theta)$ circuit except for single-qubit rotations according to the decomposition in (b). (d) False-color micrograph of the device.

An explicit design of $\mathcal{N}_H(\theta)$ as well as symmetry-preserving circuits are shown in Fig. 1(b). Since $[\mathcal{N}_H(\theta), S_{tot}^2] = 0$, to conserve the total spin s no single-qubit rotation is needed. To conserve s_z, the single-qubit operations are chosen to be z-rotations, namely, $Z_\theta = e^{-i\theta\sigma_z/2}$. Note that the s-conserving circuit readily conserves s_z. The mirror symmetry can be easily preserved by choosing the gate parameters symmetrically with respect to the middle of the chain and it may be used in combination with the other symmetries. If the initial state has mirror symmetry with $m = \pm 1$, then the symmetric choice of the parameters, as shown in Fig. 1(b), results in the output state with matching m. Note that the preservation of a symmetry operator does not imply that we know the eigenvalue for a given energy eigenvector. For instance, if the Hamiltonian preserves mirror symmetry, we know that half of the energy eigenstates have $m = +1$ and the other half have $m = -1$. However, the distribution of the symmetry eigen-

values are model dependent and even may vary by system size.

IV. ERROR MITIGATION

To diminish the effect of noise and improve the accuracy of the extracted energies, we employ the zero-noise extrapolation (ZNE) method [47–49] for error mitigation. To perform ZNE, we rescale the circuit depths by a factor of k while maintaining the same unitary. As shown in Fig. 1(c), for the parameterized circuit $U(\vec{\theta})$, every $\mathcal{N}(\theta)$ operation is divided into k consecutive repetitions of $\mathcal{N}(\theta/k)$. Such a treatment allows the noise-scaling factor k to be any positive integer. For the initialization circuit U_I, we append the $U_I U_I^\dagger$ pairs, which means k can only be odd numbered. To access more choices in k and improve the statistics, for an even-numbered k, we perform both cases of $k = 2n-1$ and $k = 2n+1$ for
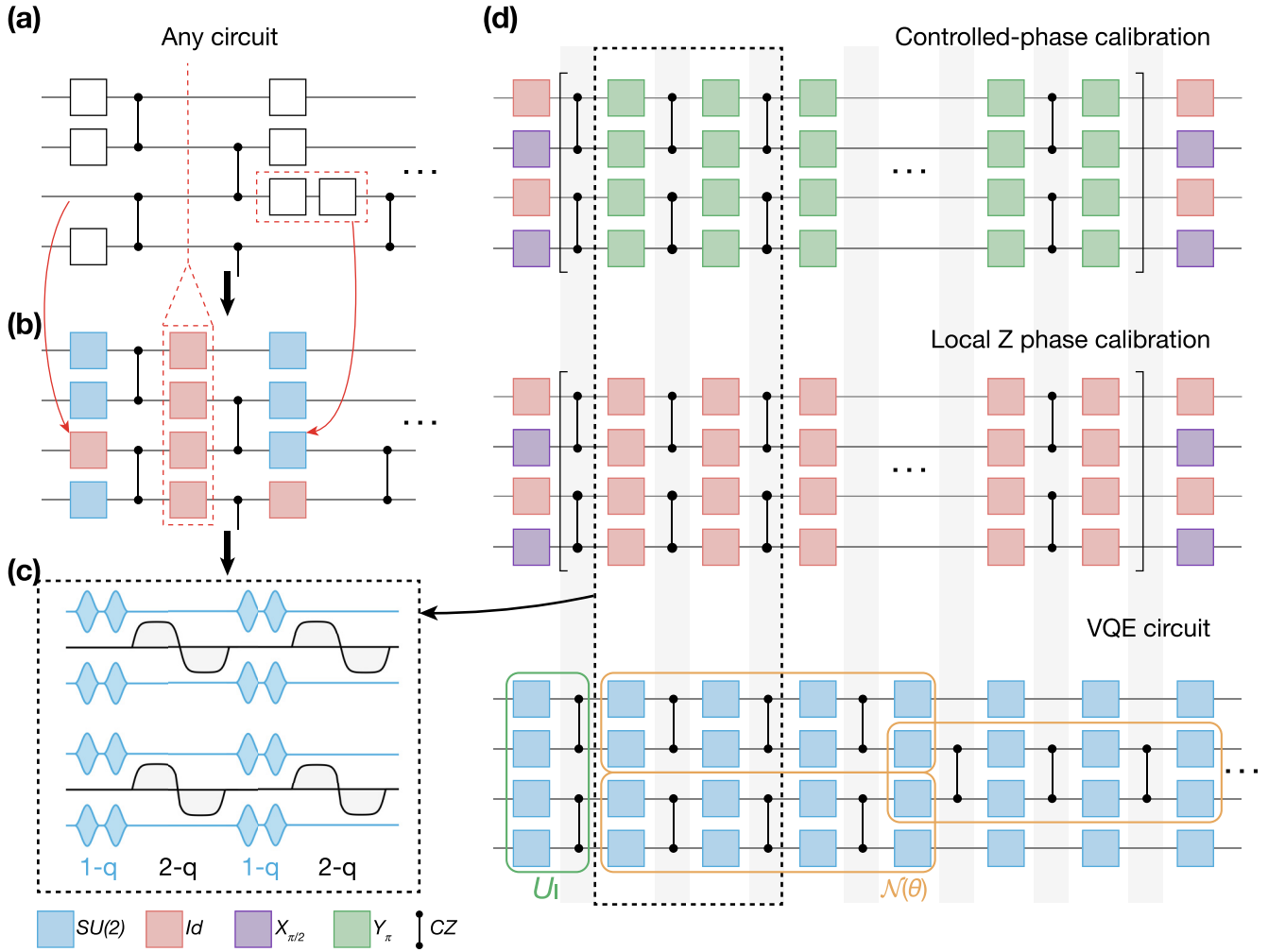
FIG. 2. Circuit compilation using the isomorphous waveform method. (a)–(c) Step-by-step compilation. An arbitrary quantum circuit composed of modular single- and two-qubit gates (a) can be rearranged into periodic single-qubit (1-q) and two-qubit (2-q) gate cycles (b). Red arrows indicate the identity filling and single-qubit gate squeeze operations. All SU(2) operations including identity operations are subsequently compiled into two $\pi/2$ pulses according to the U3 decomposition (c). (d) Gate sequences used in the controlled-phase calibration, the local Z phase calibration, and the VQE experiment for the Heisenberg model in which the initialization circuit (red solid box) and the $\mathcal{N}(\theta)$ circuit (brown solid box) are indicated. The black dashed box indicates a section of the three circuits that share a common waveform as illustrated in (c).

the initialization circuit and take the averaged outcome. After obtaining the expectation value of the Hamiltonian for each k, we employ an extrapolation method, based on either polynomial or exponential fitting, to estimate the result at $k = 0$, thereby obtaining the ZNE. In our experiment, we opted for the exponential extrapolation method as it produced the lowest fitting error and yielded results closer to the theoretical values.

V. SUPERCONDUCTING QUANTUM SIMULATOR

Our experiment is performed on a superconducting quantum processor with a ring of 16 transmon qubits [Fig. 1(d)] mounted inside a dilution refrigerator. A tunable coupler (also a transmon qubit) connects each pair of neighboring qubits and serves as an independent control knob for adjusting their coupling strength. A shared control line is used for delivering both the single-qubit gate signal to the qubit and the

two-qubit gate signal to an adjacent coupler, reducing the wiring efforts both on the chip and inside the refrigerator. More details about the device can be found in Appendix D and its eight-qubit predecessor [50]. In this experiment, we use the coupler-assisted adiabatic controlled-Z (CZ) gate [51] in conjunction with the net-zero pulsing technique to suppress dephasing from low-frequency flux noise [52]. The CZ gate fidelities when simultaneously applied are nearly 99% fidelity on average.

VI. CIRCUIT-AGNOSTIC COMPILATION AGAINST CROSSTALK

The VQE algorithms and the ZNE error mitigation often involve long circuits with parallel gate operations. It is commonly seen in practice that the performance of modular single- and two-qubit gates is inconsistent between calibration

and final implementation, as the control signals are distorted due to the spatial and temporal crosstalk effect that varies with circuits. To combat this, we implement a generally applicable compilation strategy named the *isomorphic waveform*. The key idea is to maximally match the waveforms used during calibration and subsequent implementations by rearranging an arbitrary quantum circuit into interleaved layers of single- and two-qubit gates and translating them into well-timed pulses [Figs. 2(a) to 2(c). First, for two-qubit gates that cannot be parallelized, one can always split them and insert a layer of identity gates between them (identity filling). Then, multiple concatenated single-qubit gates are squeezed into a single SU(2) operation. Note that we also perform identity filling to the "no gate" case. Now with one SU(2) operation for every qubit during each cycle, we apply the U3 decomposition [53] to compile the SU(2) operation into two physical $\pi/2$ pulses and additional virtual Z gates, resulting in restless single-qubit gate cycles. Since the virtual Z gates only affect the pulse phases, the entire waveform shape is almost identical given an arbitrary original circuit.

A direct consequence of this compiling scheme is that only the $\pi/2$ pulses are required to calibrate. More importantly, simultaneous calibration of these $\pi/2$ pulses immediately accounts for microwave signal crosstalk because all pulses have fixed shapes and hence fixed crosstalk influence; this substantially reduces the efforts for performing crosstalk compensation. In addition, the timing of both single- and two-qubit pulses, is fixed during calibration and subsequent experiments. In this way, pulse distortions — if not completely removable — can be more consistent in different circuits; this makes the gate performance more predictable for long circuits. Figure 2(d) shows the circuits used for calibrating the controlled phase and single-qubit phase correction. With the isomorphous waveform method, their compiled waveforms are almost identical to each other and to the VQE circuits. In addition, the method is compatible with randomized compiling [54], another powerful error mitigation technique. The method may require more single-qubit gates to be added to the circuits. However, this is unlikely to degrade the whole circuit fidelity due to the fact that the SU(2) squeeze operation can reduce the circuit depth and the fact that the single-qubit gate fidelities are typically much better than the two-qubit ones.

VII. FULL SPECTROSCOPY OF HEISENBERG HAMILTONIAN WITH $N = 4$

After the processor is calibrated, we implement the full energy spectroscopy of a four-qubit Heisenberg spin chain on the selected qubits [Fig. 3(a)]. Since all the eigenstates have definitive s, s_z, and m numbers, the ground state $|E_1\rangle$ must be a global singlet (i.e., $s = s_z = 0$), which we denote as $|\mathcal{S}_1\rangle = |E_1\rangle$. Next in the spectrum are two triplets (i.e., $s = 1$), each with degeneracy three corresponding to $s_z = 0, \pm 1$, which we denote as $|\mathcal{T}_1^{(0,\pm 1)}\rangle = |E_{2,3,4}\rangle$ and $|\mathcal{T}_2^{(0,\pm 1)}\rangle = |E_{5,6,7}\rangle$ (the superscript denotes the s_z number). The spectrum then follows with one more singlet $|\mathcal{S}_2\rangle = |E_8\rangle$ and one triplet $|\mathcal{T}_3^{(0,\pm 1)}\rangle = |E_{9,10,11}\rangle$. The highest-energy states are a quintuple (i.e., $s = 2$) with degeneracy five corresponding to $s_z = 0, \pm 1, \pm 2$, namely, $|\mathcal{Q}^{(0,\pm 1,\pm 2)}\rangle = |E_{12,\dots,16}\rangle$.

To solve the singlet $|\mathcal{S}_1\rangle$ which is the ground state, one can simply use the s-conserving circuit (three parameters) in combination with mirror symmetry (to subtract one parameter) illustrated in Fig. 1(b). Therefore, there are only two parameters per layer. We prepare the initial state $|\Phi\rangle = |\psi^-\rangle \otimes |\psi^-\rangle$, where $|\psi^\pm\rangle = (|01\rangle \pm |10\rangle)/\sqrt{2}$. Since the initial state has a total spin $s = 0$, the final state remains in the singlet manifold. A simple average energy minimization with single weight ($P = 1$) in the cost function (1) can estimate $E_{\mathcal{S}_1}$. The result converges to a precise value for a circuit with $L = 2$ layers. Figure 3(b) shows the convergence of the cost function versus optimization iterations and the energy estimation as a function of noise-scaling factor k. The ground-state energy extrapolated at $k = 0$ yields $E_{\mathcal{S}_1} = (-6.570 \pm 0.059)$ (theory: -6.464) assuming $J = 1$. Note that our approach requires only four parameters to train, while the widely used hardware efficient ansatz [26] requires a total of three layers and 32 parameters. As shown in Ref. [38], the situation gets worse as the system size or the number of target states in SSVQE increases.

For singlet $|\mathcal{S}_2\rangle$, we resort to the SSVQE method by training $|\mathcal{S}_1\rangle$ and $|\mathcal{S}_2\rangle$ simultaneously with double initial states ($P = 2$ in the cost function). Unlike the ground state, producing two orthogonal initial states with $s = 0$ requires long-distance controlled-NOT gates, which are not available in our device. We instead use the s_z-conserving circuit with $L = 3$ layers and two initial states $|\Phi_1\rangle = |0101\rangle$ and $|\Phi_2\rangle = |1010\rangle$. To ensure that the final states fall into the $s = 0$ manifold, an additional penalty term $\langle S_{\text{tot}}^2 \rangle$ is included in the cost function (see Appendix B for details). Due to the complex nature of the cost function, the training becomes much harder than the ground state and takes about 24 hours until convergence. We only obtain one successful convergence [Fig. 3(b)] out of a few trials as the processor performance fluctuates over time. Interestingly, we find that, in this case, the hybrid optimization of Nelder-Mead (first 14 iterations) followed by Adam performs better than either of them separately.

For the three triplet groups $\mathcal{T}_{1,2,3}$, the eigenstates can be efficiently solved with fewer training tasks by identifying symmetries in these states and choosing proper initial states. To understand this, let us focus on the case of $s_z = 0$. We use the total spin s-conserving circuit with mirror symmetry with $L = 2$ layers. For the initial state $|\Phi_1\rangle = (|0101\rangle - |1010\rangle)/\sqrt{2}$ which is determined by symmetry numbers $s = 1$, $s_z = 0$, $m = -1$, minimizing the average energy yields the lowest eigenstate in the same-symmetry manifold, which is exactly $|\mathcal{T}_1^{(0)}\rangle$. Then applying the same trained circuit on $|\Phi_2\rangle = (|0011\rangle - |1100\rangle)/\sqrt{2}$, which is orthogonal to $|\Phi_1\rangle$, but shares the same symmetries immediately generates $|\mathcal{T}_3^{(0)}\rangle$. Similarly, applying the same trained circuit on $|\Phi_3\rangle = (|0110\rangle - |1001\rangle)/\sqrt{2}$ which is orthogonal to $|\Phi_1\rangle$ and $|\Phi_2\rangle$ but with $m = +1$ unambiguously results in $|\mathcal{T}_2^{(0)}\rangle$. In this manner, all three triplet states $s_z = 0$ share a common trained circuit and error mitigation is conducted separately [Fig. 3(c)]. The same treatment also works for the manifold of $s_z = \pm 1$. In Appendix B, we give the exact form of all the initial states and their corresponding circuits.

The last manifold of the spectrum is a quintuple with $s = 2$. Two eigenstates with $s_z = \pm 2$ are easy to obtain as all the spins are aligned. Therefore, we focus on generat-
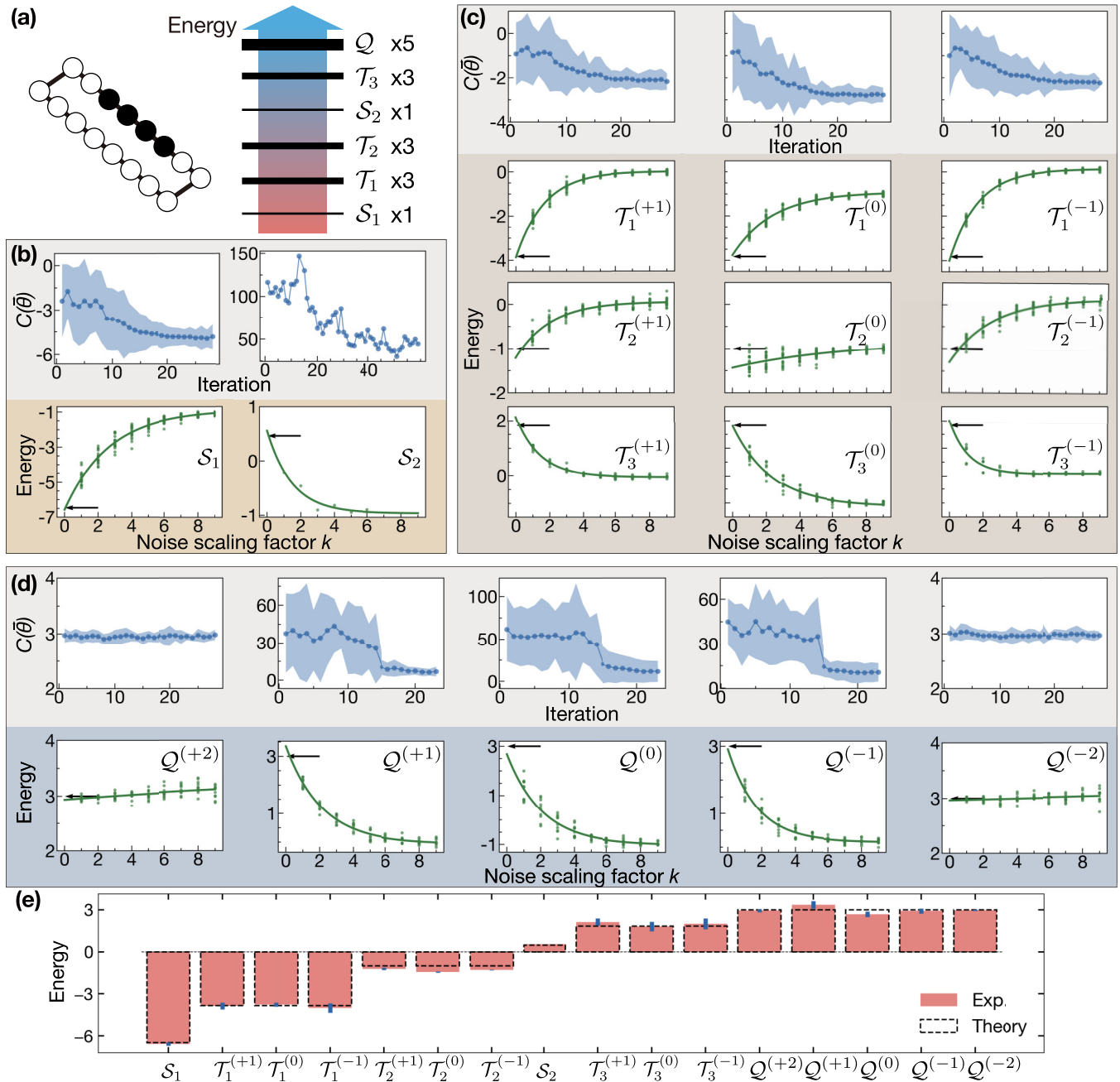
FIG. 3. Full spectroscopy of a four-qubit Heisenberg spin chain. (a) The left plot shows the device connectivity and the four active qubits (solid circles). The right plot sketches the spectrum of the 16 states of the four-qubit Heisenberg spin chain which are grouped by degeneracy. (b)–(d) VQE training and error mitigation for each of the 16 states including (b) the singlets $\mathcal{S}_1$ and $\mathcal{S}_2$, (c) the triplets $\mathcal{T}_1$, $\mathcal{T}_2$, and $\mathcal{T}_3$, and (d) the quintuple $\mathcal{Q}$. The top panels (gray background) in each figure plot the training curves of the cost function $C(\vec{\theta})$. The blue dots are the mean values of the training curves with different initial parameters. The shades indicate two times the standard deviation. The bottom panels (colored background) plot the error mitigation results for different training outcomes (green dots) and the exponential fit to their mean (green line). The black arrows indicate the theoretical values. Note that the triplet states with the same s_z values share a common trained circuit and their energies can be obtained simply by switching the initialization circuit. (e) Comparison of the extrapolated zero-noise energies (red bars) and the theoretical values (dashed boxes) for all 16 eigenstates. The error bars (blue bars) denote plus/minus two times the standard deviation. All energies are given in units of J.

ing the three eigenstates with $s_z = 0, \pm 1$. Generating initial states with total spin $s = 2$ and $s_z = 0, \pm 1$ is not easy without long-distance controlled-NOT gates. Instead, we add the penalty term $\langle (S_{\text{tot}}^2 - 6)^2 \rangle$ to the cost function with $P = 1$ to guarantee the convergence to the $s = 2$ manifold. We use

the s_z-conserving circuit and the initial states $|0101\rangle$ ($s_z = 0$), $|0111\rangle$ ($s_z = -1$), $|0001\rangle$ ($s_z = 1$). In this case, we disregard the use of mirror symmetry due to the lack of this property in the initial states. The results are shown in Fig. 3(d). Again, we find that similar to the SSVQE simulation of $|\mathcal{S}_2\rangle$ [Fig. 3(b)],
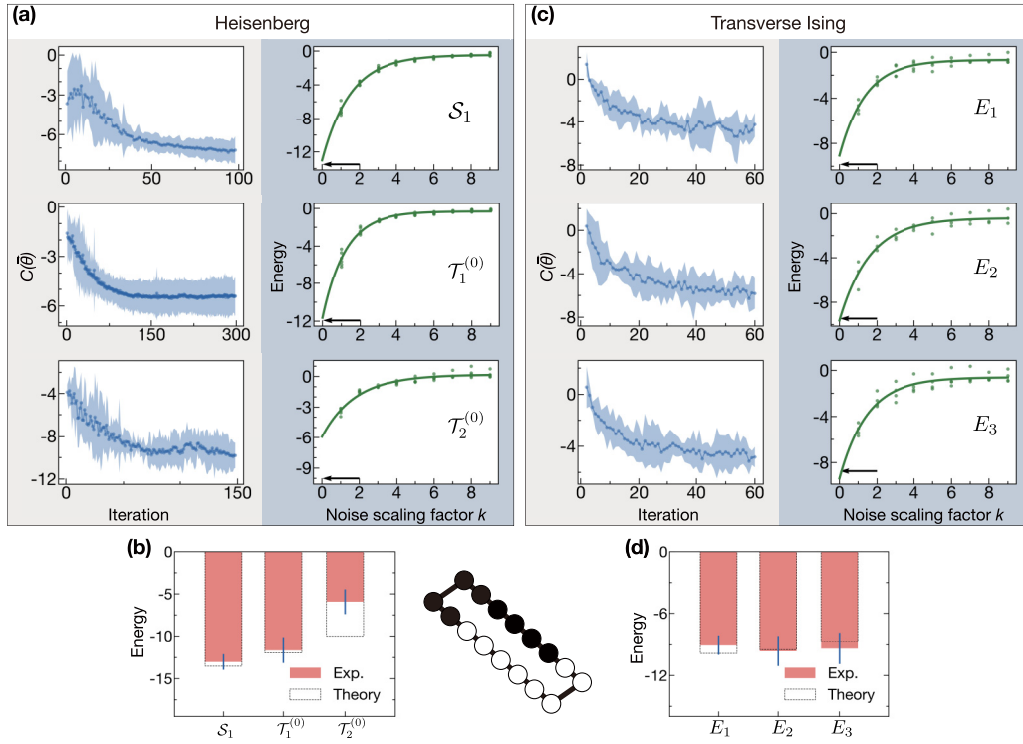
FIG. 4. Low-energy spectroscopy of an eight-qubit Heisenberg and transverse Ising chain. (a) VQE training (left panels) and error mitigation (right panels) for the three lowest eigenstates for the eight-qubit chain with the Heisenberg interactions. (b) Comparison of the extrapolated zero-noise energies (red bars) and the theoretical values (dashed box) of the Heisenberg model. The error bars (blue bars) are plus/minus two times the standard deviation from the measured values. (c) Same as (a) but with the transverse Ising interactions. (d) Same as (b) but for the Ising model. The center panel at bottom shows the eight active qubits (solid circles). All energies are given in units of J.

the hybrid optimization of the gradient-free Nelder-Mead (first 14 iterations) and gradient-based Adam method gives the best convergence. In fact, when the cost function contains several terms, the potential landscape becomes complex with multiple local minima. It is likely that a few iterations by a gradient-free optimizer, such as the Nelder-Mead, bring the cost function to the vicinity of its global minimum whereas a following gradient-based optimizer, such as Adam, facilitates the convergence. This can be seen from the immediate drop in the cost function when switching from Nelder-Mead to Adam at the 15th iteration in all the relevant cases. The estimated energy eigenvalues of all the 16 states are compared with the theory in Fig. 3(e). The average deviation is about 0.13, validating our approach for obtaining the full variational spectroscopy.

VIII. PARTIAL SPECTROSCOPY OF HEISENBERG HAMILTONIAN WITH $N = 8$

To show the scalability of our approach, we perform low-energy spectroscopy for an eight-qubit Heisenberg Hamiltonian. We consider estimating the three lowest eigenenergies, namely, $E_{\mathcal{S}_1}$, $E_{\mathcal{T}_1}$, and $E_{\mathcal{T}_2}$. For the ground state $\mathcal{S}_1$, we use the s-conserving circuit with $L = 3$ layers, and the initial state $|\Phi\rangle = |\psi^-\rangle^{\otimes 4}$. The training of the cost function ($P = 1$) and the error mitigation results are shown in Fig. 4(a). For the first excited state $\mathcal{T}_1^{(0)}$, we use the s-conserving circuit with $L = 4$ layers and the initial state $|\Phi\rangle = |\psi^-\rangle|\psi^+\rangle|\psi^-\rangle|\psi^-\rangle$. Remarkably, there are 84 CNOT gates in one cycle of the

parameterized circuit and a total of 792 CNOT gates in the error mitigation circuit with scaling factor $k = 9$. The consistency in the measured data [middle panels of Fig. 4(a)] manifests the consistency in our gate performance in large-scale circuits, owing to the isomorphous waveform technique. For other choices of s_z, one can simply change $|\psi^+\rangle$ to $|00\rangle$ or $|11\rangle$. Again, if one is interested to get both $\mathcal{T}_1^{(0)}$ and $\mathcal{T}_2^{(0)}$, simultaneously, one has to use SSVQE with $P = 2$. While one of the initial states is the same as before, the other one can be $|\Phi\rangle = |\psi^-\rangle|\psi^-\rangle|\psi^+\rangle|\psi^-\rangle$. The results are shown in the lower panels of Fig. 4(a), where the $\mathcal{T}_1^{(0)}$ trace is dropped for clarity. The three estimated eigenenergies and their theoretical values are compared in Fig. 4(b). While $E_{\mathcal{S}_1}$ and $E_{\mathcal{T}_1}$ can be estimated very precisely, the energy $E_{\mathcal{T}_2}$ shows a larger error. This is because a circuit with $L = 4$ layers is not capable to target two eigenstates simultaneously with high precision.

IX. PARTIAL SPECTROSCOPY OF TRANSVERSE ISING HAMILTONIAN WITH $N = 8$

The key advantage of programmable digital quantum simulators is their capability in simulating different Hamiltonian models. To show the versatility, we also perform on the same device the variational spectroscopy for the transverse-field Ising Hamiltonian

$$H = J \sum_{i=1}^{N-1} \sigma_x^i \sigma_x^{i+1} + h \sum_i \sigma_z^i, \tag{4}$$

where J is the coupling strength and h is the transverse field strength. This system has a critical point at $h = J$ when the ground state goes through a phase transition from an antiferromagnetic (for $J < h$) to a paramagnetic phase (for $J > h$) [43,55]. We focus on extracting the low-energy spectrum of the Hamiltonian (4) at its critical point, i.e., $J = h$, where the eigenstates are highly entangled and expected to be harder for the VQE algorithm. Note that, in digital simulation, we do not need to specify the exact value of J and h. In fact, our eigenenergies are given in units of J. The Hamiltonian commutes with two operators, namely, the mirror operator $\mathcal{M}$ and the parity operator $\Pi_z = \bigotimes_{i=1}^{N} \sigma_z^i$, which imply that every eigenstate has two symmetry numbers, $m = \pm 1$ (i.e., $\mathcal{M}|E_j\rangle = m|E_j\rangle$) and $\pi_z = \pm 1$ (i.e., $\Pi_z|E_j\rangle = \pi_z|E_j\rangle$). Hence, We can denote the state as $|E_j^{(m,\pi_z)}\rangle$. For simulating the transverse Ising Hamiltonian, the two-qubit operation $\mathcal{N}(\theta)$ is replaced with

$$\mathcal{N}_I(\theta) = e^{-i\theta\sigma_x^i\sigma_x^{i+1}/2}. \tag{5}$$

The circuit used to construct $\mathcal{N}_I(\theta)$ is depicted in Fig. 1(b). To ensure the preservation of the Π_z symmetry, the single-qubit operations should all be z-rotations. Furthermore, mirror symmetry is readily preserved by choosing parameters symmetrically with respect to the middle of the chain. The three lowest-energy eigenstates are denoted as $|E_1^{(1,1)}\rangle$, $|E_2^{(-1,-1)}\rangle$, and $|E_3^{(1,-1)}\rangle$. These three eigenstates possess symmetry numbers that allow their independent generation through the appropriate choice of the initial state and a cost function with only $P = 1$. We simulate these three eigenstates for both four-qubit and eight-qubit Ising chains, presenting the result for the eight-qubit case here. The four-qubit results and other experimental details can be found in Appendix I. We employ the π_z-conserving circuit ($L = 3$) with mirror symmetry and the initial state $|\Phi\rangle = |000\rangle|\phi_{(4,5)}\rangle|000\rangle$, where $|\phi_{(4,5)}\rangle$ represents the quantum state of qubits 4 and 5. To satisfy the desired symmetries, $|\phi_{(4,5)}\rangle$ is chosen to be one of the Bell states $|\phi^+\rangle = (|00\rangle+|11\rangle)/\sqrt{2}$, $|\psi^-\rangle$ and $|\psi^+\rangle$ for estimating E_1, E_2, and E_3, respectively. The training and error mitigation results are shown in Fig. 4(c). A good agreement between the measured energies and the theoretical values is observed [Fig. 4(d)].

X. GENERALITY

It should be noted that the results previously presented focused on the Heisenberg and Ising Hamiltonians as examples due to their well-known symmetries. However, our approach is not constrained to these two models. Indeed, combing SSVQE and exploitation of symmetries can be applied to any Hamiltonian for efficiently extracting its low-energy spectrum. In fact, there have been several attempts to exploit symmetries in various models for solving problems in condensed matter [30], quantum chemistry [35,36], and machine learning [37]. Determining the symmetry of a physical model and designing a corresponding symmetry-conserving ansatz is generally a nontrivial task. For instance, in the context of molecular models, one would typically employ methods such as the Jordan-Wigner or Bravyi-Kitaev mappings to transform a molecular Hamiltonian into qubit Hamiltonians, thereby enabling its simulation on qubit-based quantum simulators.

Specifically, when using the Jordan-Wigner transformation, which maps the occupations of orbitals to excitations of qubits, the conservation of particle numbers corresponds to the conservation of excitation in qubits. Therefore, in this case, one can utilize the s_z-conserving ansatze that we presented in the paper. Another example is time-reversal symmetry, which often arises in chemistry problems and results in strictly real eigenstates. To preserve this symmetry in a quantum circuit, one can simply apply a parameter rule to constrain the variational ansatz to only produce states that are strictly real [40].

XI. CONCLUSION

In our study, we present an experimental demonstration of multilevel variational spectroscopy using a programmable superconducting quantum simulator. To achieve such a task, we incorporate a combination of several techniques into our experiments. This includes (i) the inclusion of symmetries in the circuit design; (ii) exploiting SSVQE for targeting multiple eigenstates; (iii) introducing a circuit-agnostic waveform compilation technique for pulse optimization; and (iv) performing ZNE error-mitigation technique. Our findings highlight the resource efficiency afforded by symmetry and the ability to target a greater number of states through the implementation of the subspace search method and the inclusion of penalty terms. Additionally, we discover that a hybrid optimization strategy, which combines a gradient-free Nelder-Mead with gradient-based Adam, offers faster convergence when penalty terms are present in the cost function. This suggests that, in a disrupted potential landscape caused by relatively strong penalty terms, Nelder-Mead is less sensitive to local minima, guiding the cost function toward its global minimum. At this point, the Adam optimizer can rapidly converge.

Despite its advantages, there are several challenges that one has to address for implementing our multilevel spectroscopy method for a general system. First, a significant challenge is the circuit depth overhead, which is inherent to the SSVQE algorithm when the number of target states increases. Second, it is generally nontrivial to determine the symmetries underlying a given physical model. Third, finding the initialization circuit and variational ansatz corresponding to its symmetry properties are not routine tasks and in general model dependent. Fourth, even if one knows the initialization and the parameterized ansatzes, it is not ensured that the hardware limitations, such as limited connectivity, allows their implementation.

TABLE I. State properties and VQE information for the four-qubit and eight-qubit Heisenberg model.

Four-qubit	s	s_z	z	$\langle\hat{H}\rangle$	$C(\vec{\theta})$	No. of parameters	Optimizer	No. of CNOT[a]
$\mathcal{S}_1$	0	0	1	-6.464	$\langle\hat{H}\rangle$	4	NM[b]	18(180)
$\mathcal{S}_2$	0	0	1	0.464	$\langle\hat{C}_1\rangle$[c]	12	NM+Adam	27(243)
$\mathcal{T}_1^{(+1)}$	1	1	-1	-3.828	$\langle\hat{H}\rangle$	4	NM	18(207)
$\mathcal{T}_1^{(0)}$	1	0	-1	-3.828	$\langle\hat{H}\rangle$	4	NM	18(189)
$\mathcal{T}_1^{(-1)}$	1	-1	-1	-3.828	$\langle\hat{H}\rangle$	4	NM	18(207)
$\mathcal{T}_2^{(+1)}$	1	1	1	-1	$\langle\hat{H}\rangle$	4	NM	18(207)
$\mathcal{T}_2^{(0)}$	1	0	1	-1	$\langle\hat{H}\rangle$	4	NM	18(189)
$\mathcal{T}_2^{(-1)}$	1	-1	1	-1	$\langle\hat{H}\rangle$	4	NM	18(207)
$\mathcal{T}_3^{(+1)}$	1	1	-1	1.828	$\langle\hat{H}\rangle$	4	NM	18(207)
$\mathcal{T}_3^{(0)}$	1	0	-1	1.828	$\langle\hat{H}\rangle$	4	NM	18(189)
$\mathcal{T}_3^{(-1)}$	1	-1	-1	1.828	$\langle\hat{H}\rangle$	4	NM	18(207)
$\mathcal{Q}^{(+2)}$	2	2	1	3	$\langle\hat{H}\rangle$	2	NM	9(81)
$\mathcal{Q}^{(+1)}$	2	1	1	3	$\langle\hat{C}_2\rangle$[d]	8	NM + Adam	18(162)
$\mathcal{Q}^{(0)}$	2	0	1	3	$\langle\hat{C}_2\rangle$[d]	8	NM + Adam	18(162)
$\mathcal{Q}^{(-1)}$	2	-1	1	3	$\langle\hat{C}_2\rangle$[d]	8	NM + Adam	18(162)
$\mathcal{Q}^{(-2)}$	2	-2	1	3	$\langle\hat{H}\rangle$	2	NM	9(81)
Eight-qubit								
$\mathcal{S}_1$	0	0	1	-13.4997	$\langle\hat{H}\rangle$	12	NM	63(603)
$\mathcal{T}_1^{(0)}$	1	0	-1	-11.9289	$\langle\hat{H}\rangle$	16	NM	84(792)
$\mathcal{T}_2^{(0)}$	1	0	1	-10.0149	$\langle\hat{C}_3\rangle$[e]	16	NM	84(792)

[a]Number of CNOT gates in one cycle of parameterized circuit. In the brackets is the maximum number of CNOT gates used in error mitigation (up to nine cycles).

[b]NM = Nelder-Mead algorithm.

[c]$\langle\hat{C}_1\rangle = \omega_1(\langle\hat{H}\rangle_1 + \beta\langle\hat{S}_{\text{tot}}^2\rangle_1) + \omega_2(\langle\hat{H}\rangle_2 + \beta\langle\hat{S}_{\text{tot}}^2\rangle_2)$, $\omega_1 = 2$, $\omega_2 = 1$, $\beta = 10$.

[d]$\langle\hat{C}_2\rangle = \langle\hat{H}\rangle + \beta\langle(\hat{S}_{\text{tot}} - 6)^2\rangle$, $\beta = 5$.

[e]$\langle\hat{C}_3\rangle = \omega_1\langle\hat{H}\rangle_1 + \omega_2\langle\hat{H}\rangle_2$, $\omega_1 = 2$, $\omega_2 = 1$.

APPENDIX A: VQE TRAINING

To ensure that our convergence is accurate, we use a restricted range of the initial parameters, which are uniformly sampled from $-\pi/2$ to $\pi/2$. These parameters are used as a starting point for the VQE training procedure. The variational circuit with initial parameters is then compiled into isomorphic forms as described in the main text and further discussed in Appendixes D to F. At each iteration, the cost function is measured by measuring relevant correlation functions. To ensure accuracy, each measurement is repeated around 6000 times. Then by feeding the cost function into our classical optimizer, we obtain a new set of parameters $\vec{\theta}$. We consider three different ways for classical optimization, namely, the gradient-free Nelder-Mead, gradient-based Adam, and a hybrid of both. In the Nelder-Mead algorithm, the initial simplex is uniformly sampled from $-\pi/2$ to $\pi/2$. In the Adam optimizer, the initial parameters are also uniformly sampled from $-\pi/2$ to $\pi/2$. The configuration of Adam optimizer is chosen to be $\alpha = 0.1$ for the learning rate, $\beta_1 = 0.9$ for the exponential decay rate of the first moment, $\beta_2 = 0.999$ for the exponential decay rate of the second-moment, and finally, $\epsilon = 10^{-8}$ for numerical stability. In the hybrid optimization, we utilize the Nelder-Mead for ~15 iterations to obtain a

TABLE II. State properties and VQE information for the four-qubit and eight-qubit transverse Ising model.

Four-qubit	z	m	$\langle\hat{H}\rangle$	$C(\vec{\theta})$	No. of parameters	Optimizer	No. of CNOT
E_1	1	1	-4.759	$\langle\hat{H}\rangle$	8	NM	12(117)
E_2	-1	-1	-4.064	$\langle\hat{H}\rangle$	8	NM	12(117)
E_3	-1	1	-2.759	$\langle\hat{H}\rangle$	8	NM	12(117)
Eight-qubit							
E_1	1	1	-9.838	$\langle\hat{H}\rangle$	24	Adam	42(378)
E_2	-1	-1	-9.4689	$\langle\hat{H}\rangle$	24	Adam	42(378)
E_3	-1	1	-8.7432	$\langle\hat{H}\rangle$	24	Adam	42(378)

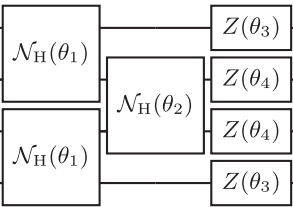TABLE III. Circuits for the four-qubit Heisenberg model.
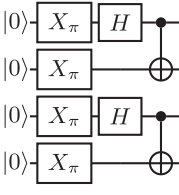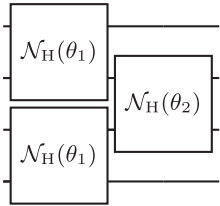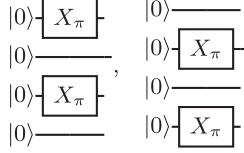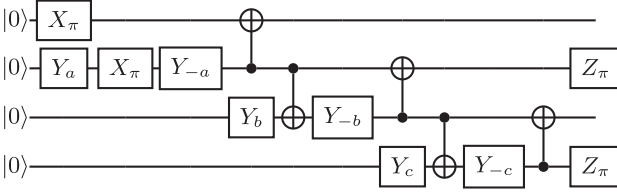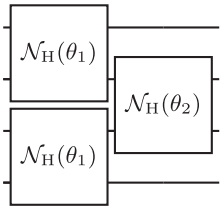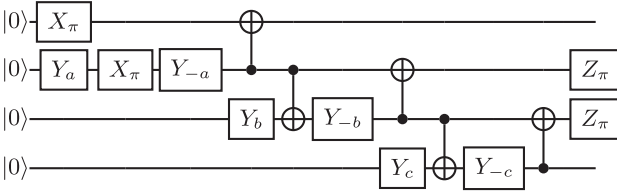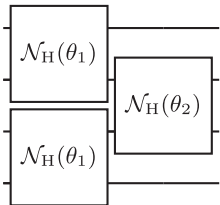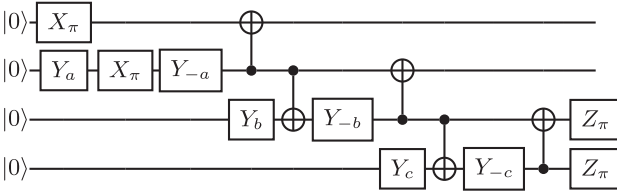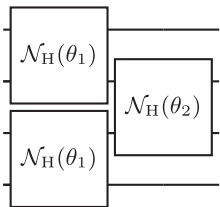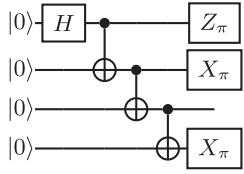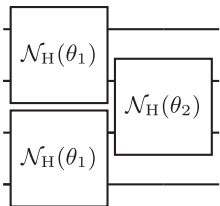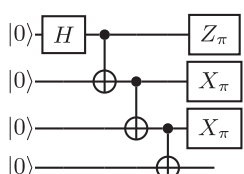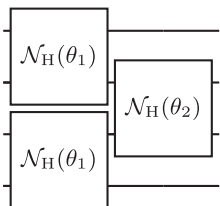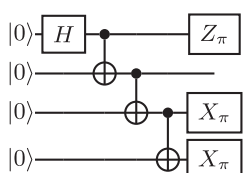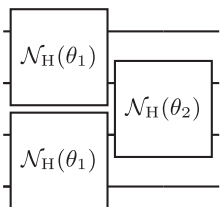
State	Initialization Circuit	Ansatz layer	No. of layers
$\mathcal{S}_1$			2
$\mathcal{S}_2$			3
$\mathcal{T}_1^{(+1)}$			2
$\mathcal{T}_2^{(+1)}$			2
$\mathcal{T}_3^{(+1)}$			2
$\mathcal{T}_1^{(0)}$			2
$\mathcal{T}_2^{(0)}$			2
$\mathcal{T}_3^{(0)}$			2

TABLE IV. Table III continued.

State	Initialization Circuit	Ansatz layer	No. of layers
$\mathcal{T}_1^{(-1)}$			2
$\mathcal{T}_2^{(-1)}$			2
$\mathcal{T}_3^{(-1)}$			2
$\mathcal{Q}^{(+2)}$			1
$\mathcal{Q}^{(+1)}$			2
$\mathcal{Q}^{(0)}$			2
$\mathcal{Q}^{(-1)}$			2
$\mathcal{Q}^{(-2)}$			1

TABLE V. Circuits for the eight-qubit Heisenberg model.

State	Initialization Circuit	Ansatz layer	No. of layers
$\mathcal{S}_1$			3
$\mathcal{T}_1^{(0)}$			4
$\mathcal{T}_2^{(0)}$			4

rough training result and then use Adam until the training converges.

In most cases, the Nelder-Mead algorithm performed better than the other two, see Tables I to II for specifying the best optimizer for every single case. However, when the cost function contains several terms, e.g., in the SSVQE with $P > 1$ or in the presence of penalizing terms, the best optimization method is often the hybrid method. This might be due to the presence of multiple local minima in such a complex potential landscape. In such cases, Nelder-Mead brings the cost function to the vicinity of its global minimum but it is slow to make the final convergence towards the exact location

of the global minimum. However, the gradient-based Adam optimizer operates well when the cost function is close to its global minimum. As a result, for complex multiterm cost functions, hybrid optimizations seem to provide faster convergence.

APPENDIX B: INITIAL STATE CONSTRUCTION

To approximate the desired eigenstate with the symmetry-preserving ansatzes in VQE, the initialization needs to be carefully chosen for the corresponding symmetry. For the Heisenberg Hamiltonian with system size $N = 4$, the two singlet eigenvectors $|\mathcal{S}_{1,2}\rangle$ share the symmetry of total spin $s = 0$,

TABLE VI. Circuits for the four-qubit transverse Ising model.

State	Initialization Circuit	Ansatz layer	No. of layers
E_1	$\lvert0\rangle$ —— ; $\lvert0\rangle$ —H—•— ; $\lvert0\rangle$ —⊕— ; $\lvert0\rangle$ ——	$\mathcal{N}_\mathrm{I}(\theta_1)$, $\mathcal{N}_\mathrm{I}(\theta_1)$, $\mathcal{N}_\mathrm{I}(\theta_2)$, $Z(\theta_3)$, $Z(\theta_4)$, $Z(\theta_4)$, $Z(\theta_3)$	2
E_2	$\lvert0\rangle$ —— ; $\lvert0\rangle$ —H—•—Z— ; $\lvert0\rangle$ —X—⊕— ; $\lvert0\rangle$ ——	$\mathcal{N}_\mathrm{I}(\theta_1)$, $\mathcal{N}_\mathrm{I}(\theta_1)$, $\mathcal{N}_\mathrm{I}(\theta_2)$, $Z(\theta_3)$, $Z(\theta_4)$, $Z(\theta_4)$, $Z(\theta_3)$	2
E_3	$\lvert0\rangle$ —— ; $\lvert0\rangle$ —H—•— ; $\lvert0\rangle$ —X—⊕— ; $\lvert0\rangle$ ——	$\mathcal{N}_\mathrm{I}(\theta_1)$, $\mathcal{N}_\mathrm{I}(\theta_1)$, $\mathcal{N}_\mathrm{I}(\theta_2)$, $Z(\theta_3)$, $Z(\theta_4)$, $Z(\theta_4)$, $Z(\theta_3)$	2

z-magnetization $s_z = 0$, and mirror symmetry $m = 1$. To target $\lvert\mathcal{S}_{1,2}\rangle$, two initial states with these symmetry numbers are required. These states can be obtained by Clebsch-Gordan decomposition as $\lvert\psi^-\rangle \otimes \lvert\psi^-\rangle$ and $\frac{\sqrt{3}}{6}(\lvert0101\rangle + \lvert1010\rangle + \lvert0110\rangle + \lvert1001\rangle - 2\lvert1100\rangle - 2\lvert0011\rangle)$. The initialization circuit for the first can be easily obtained which is depicted in Table III. However, the second requires a nontrivial initialization circuit with long-distance controlled-NOT gates which is not available in our device. Therefore, we use initial states $\lvert0101\rangle$ and $\lvert1010\rangle$, see their corresponding quantum circuits in Table III, with s_z-conserving circuit to approximate $\mathcal{S}_2$ using SSVQE.

The three triplets $\lvert\mathcal{T}_{1,2,3}^{(0,\pm1)}\rangle$ share the symmetry of total spin $s = 1$. Each of these eigenstates is triply degenerate with $s_z = 0, \pm1$. The corresponding mirror symmetry are $m = -1$ for $\lvert\mathcal{T}_{1,3}^{(0,\pm1)}\rangle$, and $m = +1$ for $\lvert\mathcal{T}_2^{(0,\pm1)}\rangle$. Therefore, for each given s_z, we use the following initial states:

$$\text{For } s_z = 0 : \begin{cases} \lvert\Phi_1\rangle = (\lvert0101\rangle - \lvert1010\rangle)/\sqrt{2}, \\ \lvert\Phi_2\rangle = (\lvert0110\rangle - \lvert1001\rangle)/\sqrt{2}, \\ \lvert\Phi_3\rangle = (\lvert0011\rangle - \lvert1100\rangle)/\sqrt{2}, \end{cases}$$

$$\text{For } s_z = +1 : \begin{cases} \lvert\Phi_1\rangle = (\lvert0001\rangle - \lvert0010\rangle + \lvert0100\rangle - \lvert1000\rangle)/2, \\ \lvert\Phi_2\rangle = (\lvert0001\rangle - \lvert0010\rangle - \lvert0100\rangle + \lvert1000\rangle)/2, \\ \lvert\Phi_3\rangle = (\lvert0001\rangle + \lvert0010\rangle - \lvert0100\rangle - \lvert1000\rangle)/2, \end{cases}$$

$$\text{For } s_z = -1 : \begin{cases} \lvert\Phi_1\rangle = (\lvert0111\rangle - \lvert1011\rangle + \lvert1101\rangle - \lvert1110\rangle)/2, \\ \lvert\Phi_2\rangle = (\lvert0111\rangle - \lvert1011\rangle - \lvert1101\rangle + \lvert1110\rangle)/2, \\ \lvert\Phi_3\rangle = (\lvert0111\rangle + \lvert1011\rangle - \lvert1101\rangle - \lvert1110\rangle)/2. \end{cases}$$

The quantum circuits for generating these states are shown in Tables III and IV.

For the quintuple $\lvert\mathcal{Q}^{(0,\pm1,\pm2)}\rangle$, which is determined by total spin $s = 2$, there are five degenerate eigenstates given by $s_z = -2, -1, 0, +1, +2$. To generate these eigenstates, we use an s_z-conserving circuit together with a penalty term added to the cost function; see the main text for more details. Therefore, the initial states for these five eigenstates are simply set to be $\lvert1111\rangle, \lvert0111\rangle, \lvert0101\rangle, \lvert0001\rangle, \lvert0000\rangle$. The corresponding initialization circuits are shown in Table IV. It should be noted that the initial states do not have mirror symmetry. Nonetheless, we use antisymmetric parameters in the circuit for $\lvert\mathcal{Q}^{(0,\pm1)}\rangle$, which does not preserve mirror symmetry, but reduce the number of parameters to train.

In the case of Heisenberg Hamiltonian with system size $N = 8$, we simulate the three lowest eigenenergies. Similar to the $N = 4$ case, the ground state $\lvert\mathcal{S}_1\rangle$ is a global singlet with total spin $s = 0$, z-magnetization $s_z = 0$, and mirror symmetry $m = 1$. The initial state for the ground state is $\lvert\psi^-\rangle^{\otimes4}$. For the first excited state $\lvert\mathcal{T}_1^{(0)}\rangle$ with $s = 1, s_z = 0, m = -1$, the initial state is set to be $\lvert\psi^-\rangle\lvert\psi^+\rangle\lvert\psi^-\rangle\lvert\psi^-\rangle$. Since the second excited state $\lvert\mathcal{T}_2^{(0)}\rangle$ share the same symmetry numbers as the first excited state, its initial state can similarly choose as $\lvert\psi^-\rangle\lvert\psi^-\rangle\lvert\psi^+\rangle\lvert\psi^-\rangle$. The initialization circuits for these three initial states are shown in Table V. For other eigenstates with $s_z = \pm1$, one can simply replace $\lvert\psi^+\rangle$ with $\lvert00\rangle$ or $\lvert11\rangle$. The circuits are not shown, as they can be easily obtained by replacing the circuit for $\lvert\psi^+\rangle$ with the circuit for $\lvert00\rangle$ or $\lvert11\rangle$.

The symmetry numbers for the low-energy spectrum of Ising Hamiltonian with four-qubit and 8eight-qubit systems are the same. Namely, the ground state $\lvert E_1\rangle$ is determined by $z = 1$ for the parity operator Π_z and $m = +1$ for mirror symmetry $\mathcal{M}$. Hence, its initial state for both system sizes $N = 4$ and $N = 8$ is set to be $\lvert0\rangle^{\otimes\frac{N-2}{2}}\lvert\phi^+\rangle\lvert0\rangle^{\otimes\frac{N-2}{2}}$. The second

TABLE VII. Circuits for the eight-qubit transverse Ising model.

State	Initialization Circuit	Ansatz layer	No. of layers
E_1			3
E_2			3
E_3			3

eigenstate, $|E_2\rangle$, exhibits $z = -1$ and $m = -1$ symmetries, with the initial state given by $|0\rangle^{\otimes\frac{N-2}{2}}|\psi^-\rangle|0\rangle^{\otimes\frac{N-2}{2}}$. The third eigenstate, $|E_3\rangle$, has $z = -1$ and $m = +1$ symmetries, and its initial state is expressed as $|0\rangle^{\otimes\frac{N-2}{2}}|\psi^+\rangle|0\rangle^{\otimes\frac{N-2}{2}}$. The initialization circuits for these three eigenstates are shown in Tables VI and VII.

APPENDIX C: ERROR MITIGATION

In our experiment, we utilize the initialization circuits to prepare initial states that satisfy the corresponding S_z value and ansatz circuits to conserve S_z. To ensure that the conser-

vation of S_z is maintained, we remove the data that fail to meet this criterion.

To mitigate errors, we employ the zero-noise extrapolation (ZNE) technique, which involves proportionally increasing the entire circuit error. For the initialization circuit U_I, we increase the circuit error by a factor of k (where $k = 2n+1$ is an odd number) by replacing the circuit U_I with $(U_I U_I^\dagger)^n U_I$. However, if $k = 2n$, we take the average of $(U_I U_I^\dagger)^{n-1} U_I$ and $(U_I U_I^\dagger)^n U_I$ to obtain the desired results. For the ansatz circuits, we can increase the circuit error by a factor of k by substituting the original $N(\theta)$ with $N(\theta/k)^k$. Such a protocol allows us to utilize even noise-scaling factors, improving
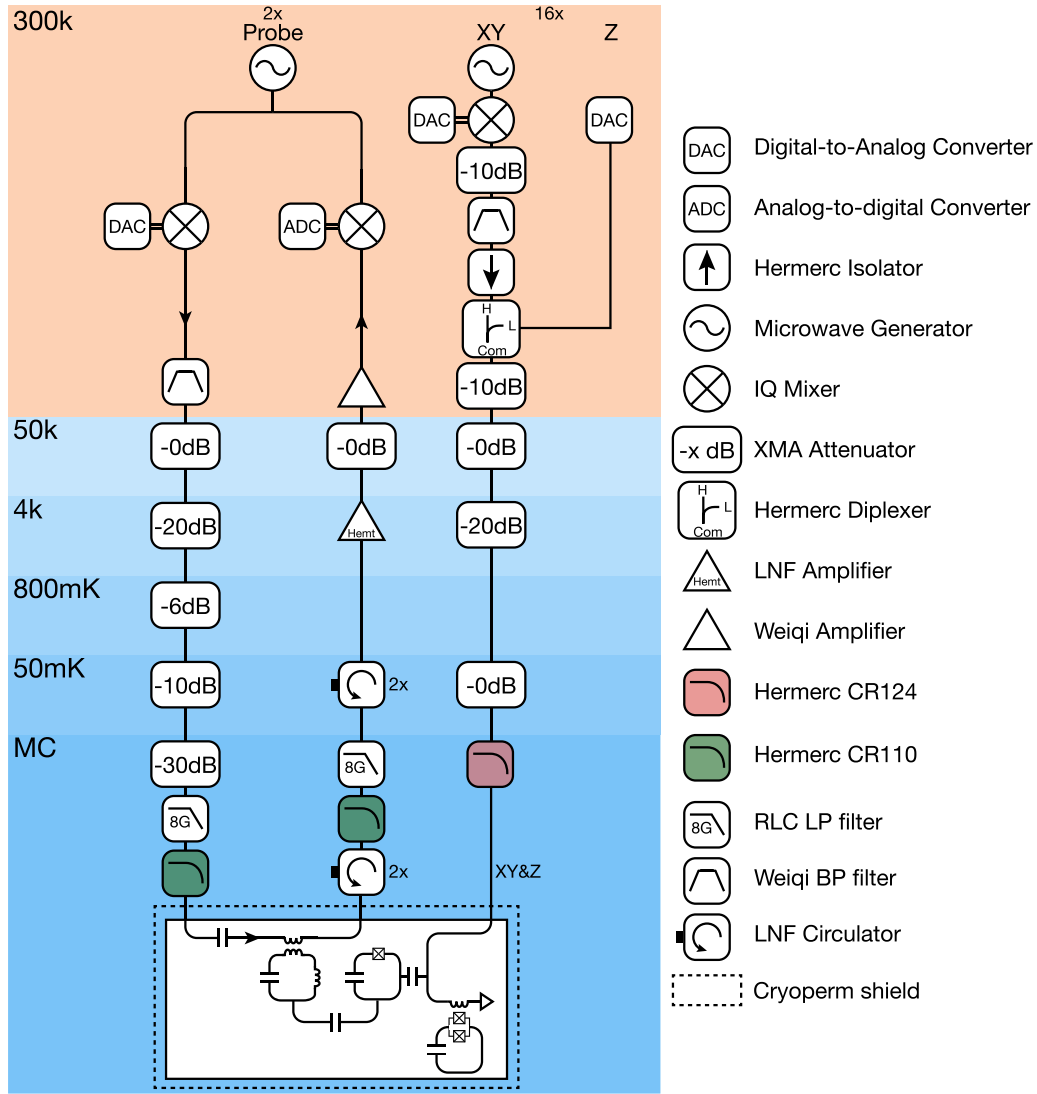
FIG. 5. Schematic diagram of the measurement setup. One set of the readout resonator, qubit, tunable coupler, the shared control line, and corresponding wiring is shown.

the statistics during extrapolation given a limited circuit length.

APPENDIX D: DEVICE MEASUREMENT SETUP

The processor is made of aluminum on sapphire using a recipe similar to that in Ref. [50] and bonded in an aluminum sample box which is then mounted inside a Blufors LD400 dilution refrigerator with a base temperature of about 12 mK. The sample box is shielded by two layers of cryoperm cylinders. Figure 5 depicts the schematic diagram of the measurement setup.

The qubits have alternating frequencies between 3.8 GHz and 4.2 GHz, designed for suppressing residual ZZ interactions. The couplers idle at their maximum frequencies of 6.4 GHz and their couplings to the qubits are about 100 MHz. The readout resonators designed at ∼7 GHz have photon loss rates of 1 MHz and a dispersive shift of 0.6 MHz. Eight resonators share a common transmission line to which a 20

fF capacitor is added at the input end to prevent photons from entering this port.

The XY microwave signal for single-qubit gates is synthesized by up-converting intermediate-frequency signals with a single-tone microwave carrier using an IQ mixer. To ensure high signal quality without reflections and spurious frequencies, an isolator and a band-pass filter are used. The fast Z signal for two-qubit gates is combined with the XY signal using a diplexer at room temperature. The combined signal is then attenuated and filtered at multiple cold stages of the DR for noise suppression. A custom-made low-pass IR filter is added to each control line at the mixing-chamber stage which attenuates signals at the qubit frequency by approximately 25 dB while allowing low-frequency signals to pass through.

The multiplexed readout signal is generated from upconversion using an IQ mixer, filtered by a 7-GHz band-pass filter, and attenuated at different temperature stages before entering the device. The output signal is sequentially amplified by a HEMT amplifier at 4 K and an amplifier at room
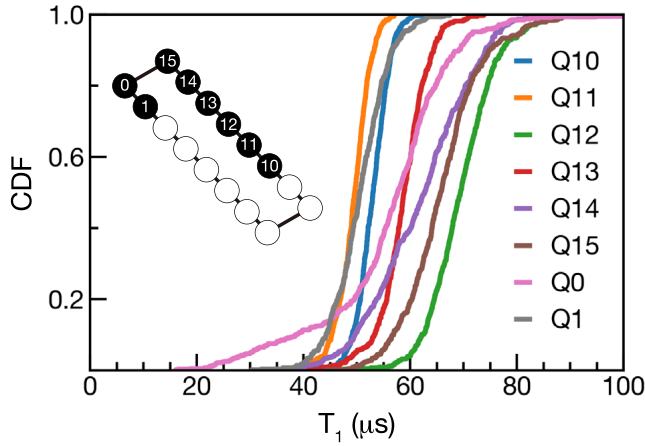
FIG. 6. Qubit T_1 time. Cumulative distribution of the repeated measured T_1 relaxation times for the selected eight qubits (inset).
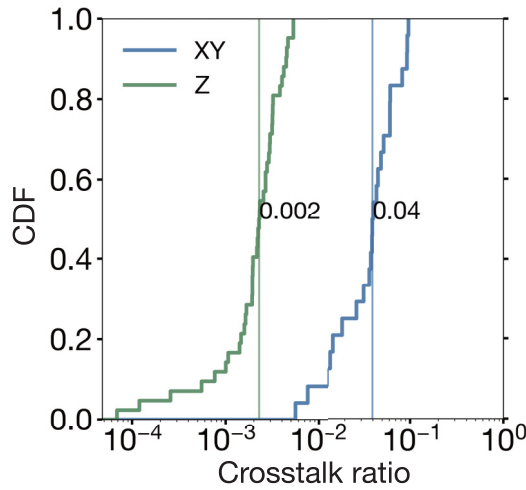

FIG. 7. Crosstalk characterization. Cumulative distribution of measured microwave (XY) and flux (Z) crosstalk ratios with the median values indicated.
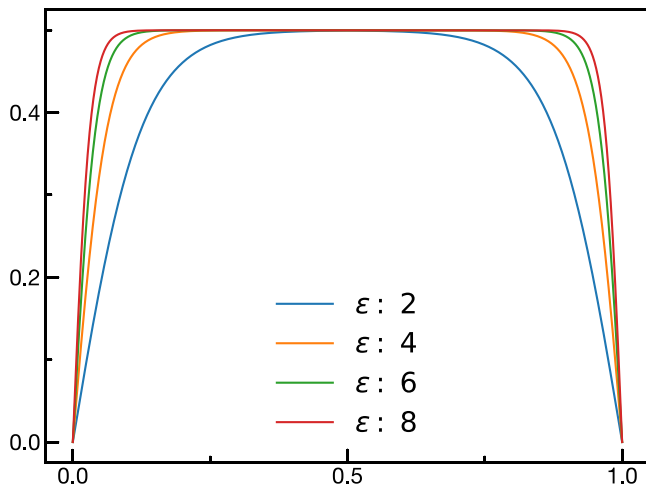

FIG. 8. CZ pulse shape. The unipolar hyperbolic tangent pulse with different values for the edge parameter ϵ.
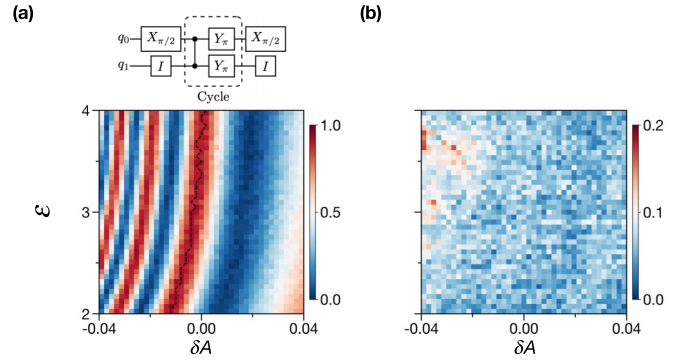

FIG. 9. CZ pulse shape and leakage. (a) The measured populations of the target qubit q_0 versus the shape parameter ϵ and the pulse amplitude δA referenced to a certain value under the echoed CZ pulse train sequence shown above. Here the number of repeated cycles is 4. The red fringe in the middle corresponds to a controlled phase of π. (b) The measured populations of the control qubit q_1 under the same sequence described in (a). The region with more population (red) indicates more leakage.

temperature before being down-converted and demodulated. To block noise from higher-temperature stages, circulators and filters are used at the output port.

The repeated characterization result of the T_1 relaxation time is shown in Fig. 6. The T_1 times of the eight selected qubits used in our experiment generally range from 40 µs to 80 µs, each showing a typical fluctuation of 10–20 µs. The average flux fluctuation in our device is estimated to be approximately 60 $\mu\Phi_0$. The measured ZZ interaction between neighboring qubits is around 10 kHz and therefore considered negligible. More device details are listed in Table VIII.
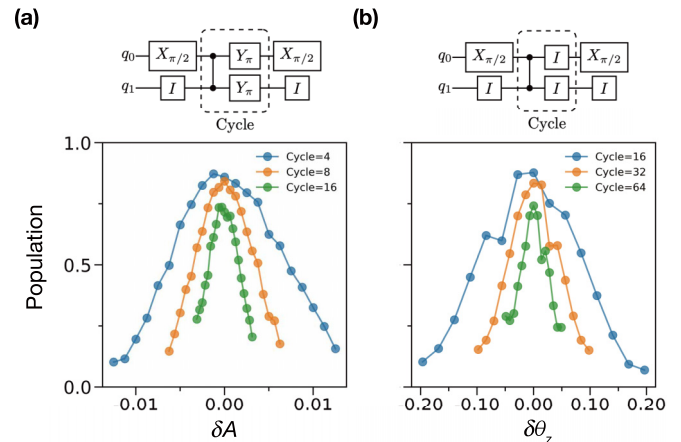

FIG. 10. Controlled phase and local Z phase calibration. (a) Progressive tuning of the pulse amplitude with respect to the controlled phase calibration with an increasing number of cycles. On the top is the calibration circuit. (b) Progressive tuning of the local Z phase correction induced by the CZ pulse with an increasing number of cycles. On the top is the calibration circuit.
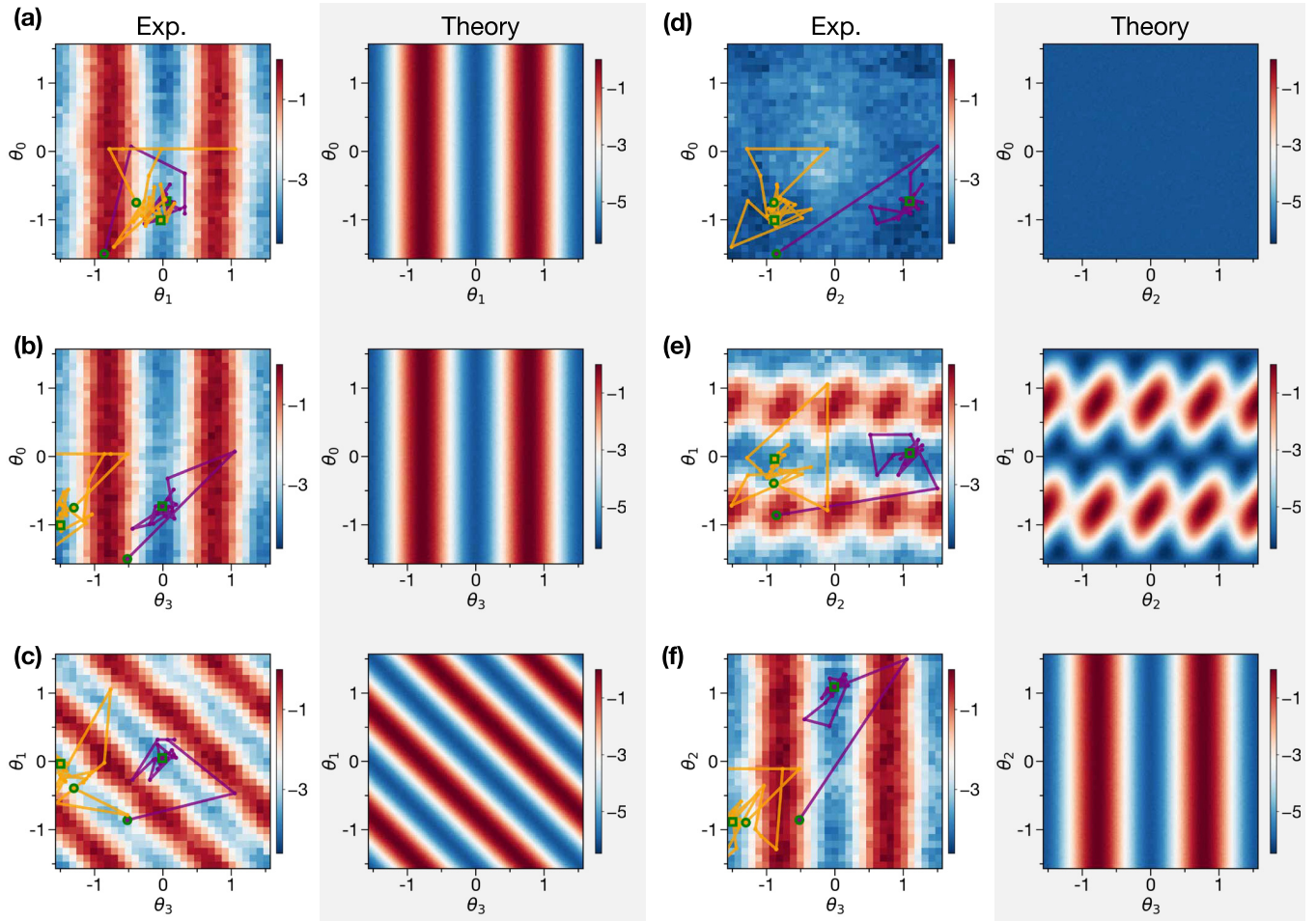
FIG. 11. Energy landscape of the $\mathcal{S}_1$ state in the four-qubit Heisenberg model. (a)–(f) The measured and theoretical values of the cost function in the $\mathcal{S}_1$ case as a function of different pairs of variational parameters selected from the set $\{\theta_0, \theta_1, \theta_2, \theta_3\}$. On the figures are plotted two convergence trajectories (orange and magenta).

TABLE VIII. Device parameters and gate fidelities.

Qubit	Q_{10}[a]	Q_{11}[a]	Q_{12}[a]	Q_{13}[a]	Q_{14}	Q_{15}	Q_0	Q_1
Cavity frequency (GHz)	6.928	7.093	6.968	7.122	6.998	7.172	6.895	7.052
Qubit frequency (GHz)	3.704	4.221	3.799	4.219	3.705	4.235	3.780	4.223
Anharmonicity (MHz)	-213.0	-203.4	-211.5	-202.8	-212.8	-204.5	-211.2	-201.4
Dispersive shift of $|1\rangle$ (MHz)	0.6	0.6	0.6	0.45	1	0.5	0.6	0.5
One-qubit gate error (simul.)(%)	0.21	0.63	0.53	0.32	0.15	0.95	0.25	0.89
Lifetime, T_1 (µs)	53	49	69	58	61	65	54	50
Ramsey decay time, T_2[a] (µs)	8	22	7	6	7	11	12	15
Echo decay time, T_{2E} (µs)	20	29	20	19	24	22	30	19
Readout fidelity of $|0\rangle$(%)	0.927	0.940	0.901	0.926	0.861	0.942	0.924	0.944
Readout fidelity of $|1\rangle$[b] (%)	0.886	0.925	0.887	0.879	0.843	0.888	0.868	0.896
Coupler (Group A)	C_{10-11}		C_{12-13}		C_{14-15}		C_{00-01}	
CZ gate error (simul.)(%)	0.96		0.69		1.24		1.33	
ZZ[c] (kHz)	10.4		12.2		15.3		12.2	
Coupler (Group B)		C_{11-12}		C_{13-14}		C_{15-00}		
CZ gate error (simul.)(%)		2.12		0.99		1.24		
ZZ[c] (kHz)		10.0		10.5		9.5		

[a]Qubits used in the four-qubit experiment. See Fig. 6 for the indexing information of the qubits.

[b]Both the $|2\rangle$ and $|1\rangle$ states are treated as the $|1\rangle$ state with the shelving protocol.

[c]The ZZ interaction strength between neighboring qubits is measured when couplers are biased at their idling point.

APPENDIX E: SINGLE-QUBIT GATES

The microwave signal or XY crosstalk is a major source of errors when performing parallel single-qubit gates. In our experiment, we use a hybrid strategy to combat the XY crosstalk. For qubits with significant crosstalk and with frequencies close to each other (usually the next-nearest-neighbor qubits), we calibrate and add the compensation signal for crosstalk cancellation [56]. Aside from those, we rely on the isomorphous waveform strategy presented in the main text which compiles the circuit into restless single-qubit cycles and automatically corrects for crosstalk. The flux or Z crosstalk can be effectively canceled by adding compensating signals. The statistics of both XY and Z crosstalk—4% for XY and 0.2% for Z (median value)—in our device are shown in Fig. 7.

For single-qubit gates, we employ the U3 decomposition [53] with the need for calibrating $X_{\pi/2}$ pulses only. We use 30-ns-long $X_{\pi/2}$. We add an additional 10-dB attenuation at room temperature to rescale the pulse amplitudes to approximately half of the maximum digital-to-analog converter (DAC) output range for better signal quality. To simultaneously calibrate these $X_{\pi/2}$ gates, we use the pulse train technique which progressively tunes up the pulse amplitude and drag coefficients with increasing cycle number. We characterize our calibrated single-qubit gate errors using simultaneous cross-entropy benchmarking (XEB), with the result shown in Table VI. The simultaneous single-qubit gate fidelities are limited by T_2 times and residual crosstalk effect.

APPENDIX F: TWO-QUBIT GATES

The CNOT gates used in our experiment are synthesized from native CZ gates and single-qubit gates. We use the coupler-assisted adiabatic CZ gate scheme demonstrated in our previous work [51]. The bipolar net-zero pulse technique is used here for improving robustness against low-frequency flux noise and minimizing signal distortion. For a unipolar half, we employ a hyperbolic tangent pulse shape described by

$$V(t) = A \frac{\tanh[4\epsilon(1/2 - |t|/\tau)]}{\tanh(2\epsilon)}, \quad -\tau/2 < t < \tau/2, \quad \text{(F1)}$$

where A and τ are the pulse amplitude and width, respectively. ϵ is a parameter controlling pulse shape. Pulse profiles with different ϵ parameters are shown in Fig. 8. A larger ϵ value tends to make the pulse rise more rapidly and hence less adiabatic. In our setup, we set all the CZ pulse duration to $60 + 60$ ns ($\tau = 60$ ns for each pole) as a trade-off between leakage and decoherence errors.

During the CZ gate calibration, we first calibrate the flux signal (Z) distortion and use inverse-infinite impulse response (IIR) filters to predistort our pulses. Then, we calibrate the flux (Z) crosstalk among different control lines and cancel it with a compensation pulse. The shape parameter ϵ is decided by performing the echoed CZ pulse train as a function of ϵ and pulse amplitude A [Figs. 9(a) and 9(b)]. The control qubit population reveals the information about the controlled phase while the target qubit population reveals the information about
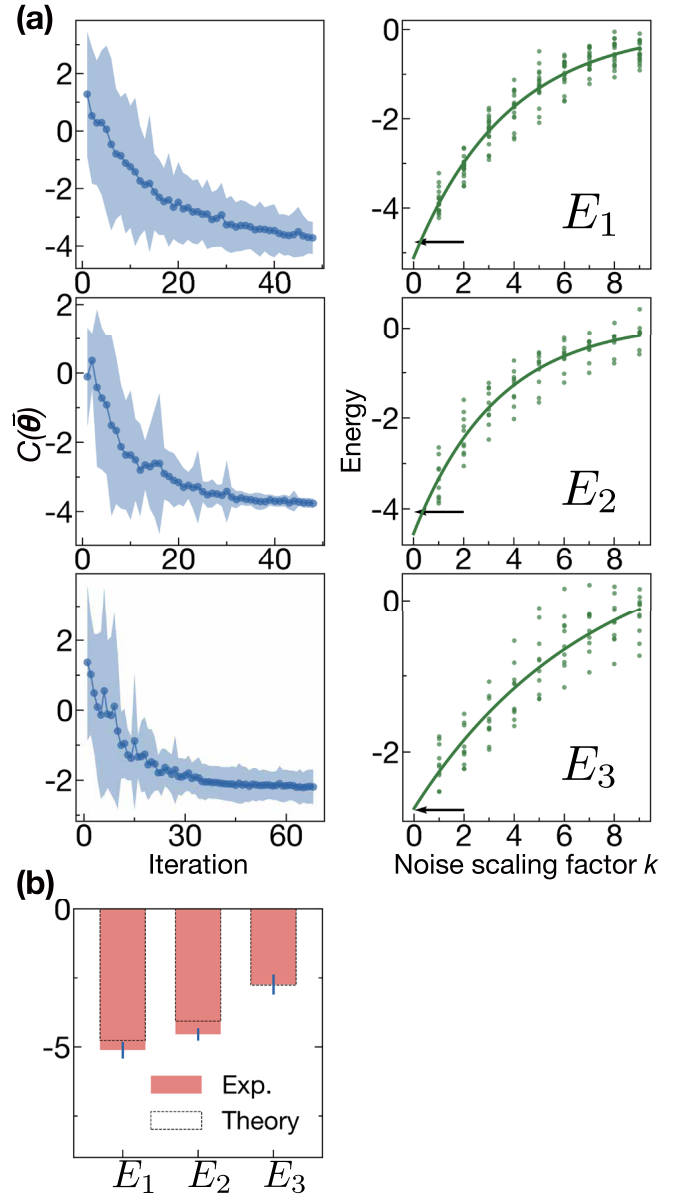

FIG. 12. Low-energy spectroscopy of a four-qubit Ising spin chain. (a) VQE training (left panels) and error mitigation (right panels) for the three lowest eigenstates for the four-qubit chain with the transverse Ising interactions. (b) Comparison of the extrapolated zero-noise energies (red bars) and the theoretical values (dashed box) of the transverse Ising model. The error bars (blue bars) are plus/minus two times the standard deviation from the measured values.

the leakage. Monitoring both helps us determine the appropriate value for ϵ. Here we choose $\epsilon \approx 2$ in our experiment.

Once the shape of the CZ pulse is determined, the only left pulse parameter to calibrate is the pulse amplitude A, which can be progressively tuned using the same echoed pulse train sequence [Fig. 10(a)]. A similar procedure is followed to obtain the local Z phase correction for both qubits [Fig. 10(b)]. Note that we divide the CZ gates in the eight-qubit chain into two groups (Table VIII). These calibrations are simultaneously performed for qubit pairs in the same group. The calibrated CZ gates are simultaneously benchmarked using

parallel two-qubit XEB. The average gate fidelities are approximately 0.99 after subtracting the single-qubit gate errors (Table VIII).

APPENDIX G: READOUT

To improve the fidelity of the readout, we employ the shelving technique as described in Ref. [57]. This method involves the addition of extra π_{ef} pulses to all qubits before executing the measurement pulse. When the demodulated signal falls within the $|e\rangle$ or $|f\rangle$ region, it is regarded as the $|e\rangle$ state. Consequently, any finite relaxation from the $|f\rangle$ to the $|e\rangle$ state during the readout pulse does not contribute to single-shot readout errors. The π_{ef} pulses are calibrated concurrently, with a pulse width of 200 ns. The readout correction matrix is determined by preparing all the 2^N computational states and measuring the probability of each resulting outcome.

APPENDIX H: POTENTIAL LANDSCAPE

To validate the accuracy of our convergence, we use the four-qubit Heisenberg state S_1 as an example. The measured potential profiles are compared to theory for six different pairs of θ (four parameters) in Figs. 11(a) to 11(f). On these figures, we also plot trajectories of two convergence traces, showing how they reach the minimum in all these dimensions.

APPENDIX I: FOUR-QUBIT ISING MODEL

Figure 12 shows the experimental results for the four-qubit transverse Ising model. With similar training and error mitigation procedures, we obtain the three lowest-energy states E_1, E_2, and E_3. The circuits used in the experiment are listed in Table VI.

[1] K. M. Jones, E. Tiesinga, P. D. Lett, and P. S. Julienne, Ultracold photoassociation spectroscopy: Long-range molecules and atomic scattering, Rev. Mod. Phys. **78**, 483 (2006).

[2] O. Fischer, M. Kugler, I. Maggio-Aprile, C. Berthod, and C. Renner, Scanning tunneling spectroscopy of high-temperature superconductors, Rev. Mod. Phys. **79**, 353 (2007).

[3] D. N. Basov, M. M. Fogler, A. Lanzara, F. Wang, and Y. Zhang, Colloquium: graphene spectroscopy, Rev. Mod. Phys. **86**, 959 (2014).

[4] R. Ulbricht, E. Hendry, J. Shan, T. F. Heinz, and M. Bonn, Carrier dynamics in semiconductors studied with time-resolved terahertz spectroscopy, Rev. Mod. Phys. **83**, 543 (2011).

[5] I. Bloch and M. Greiner, The superfluid-to-Mott insulator transition and the birth of experimental quantum simulation, Nat. Rev. Phys. **4**, 739 (2022).

[6] B. P. Lanyon, C. Hempel, D. Nigg, M. Müller, R. Gerritsma, F. Zähringer, P. Schindler, J. T. Barreiro, M. Rambach, G. Kirchmair, M. Hennrich, P. Zoller, R. Blatt, and C. F. Roos, Universal digital quantum simulation with trapped ions, Science **334**, 57 (2011).

[7] J. Zhang, G. Pagano, P. W. Hess, A. Kyprianidis, P. Becker, H. Kaplan, A. V. Gorshkov, Z.-X. Gong, and C. Monroe, Observation of a many-body dynamical phase transition with a 53-qubit quantum simulator, Nature (London) **551**, 601 (2017).

[8] J. Li, R. Fan, H. Wang, B. Ye, B. Zeng, H. Zhai, X. Peng, and J. Du, Measuring out-of-time-order correlators on a nuclear magnetic resonance quantum simulator, Phys. Rev. X **7**, 031011 (2017).

[9] J. Wang, S. Paesani, R. Santagati, S. Knauer, A. A. Gentile, N. Wiebe, M. Petruzzella, J. L. O'Brien, J. G. Rarity, A. Laing, and M. G. Thompson, Experimental quantum Hamiltonian learning, Nat. Phys. **13**, 551 (2017).

[10] H.-S. Zhong, H. Wang, Y.-H. Deng, M.-C. Chen, L.-C. Peng, Y.-H. Luo, J. Qin, D. Wu, X. Ding, Y. Hu, P. Hu, X.-Y. Yang, W.-J. Zhang, H. Li, Y. Li, X. Jiang, L. Gan, G. Yang, L. You, Z. Wang *et al.*, Quantum computational advantage using photons, Science **370**, 1460 (2020).

[11] J. Carolan, M. Mohseni, J. P. Olson, M. Prabhu, C. Chen, D. Bunandar, M. Y. Niu, N. C. Harris, F. N. C. Wong, M. Hochberg, S. Lloyd, and D. Englund, Variational quantum unsampling on a quantum photonic processor, Nat. Phys. **16**, 322 (2020).

[12] A. Keesling, A. Omran, H. Levine, H. Bernien, H. Pichler, S. Choi, R. Samajdar, S. Schwartz, P. Silvi, S. Sachdev, P. Zoller, M. Endres, M. Greiner, V. Vuletić, and M. D. Lukin, Quantum kibble–zurek mechanism and critical dynamics on a programmable Rydberg simulator, Nature (London) **568**, 207 (2019).

[13] Y. Salathé, M. Mondal, M. Oppliger, J. Heinsoo, P. Kurpiers, A. Potočnik, A. Mezzacapo, U. Las Heras, L. Lamata, E. Solano, S. Filipp, and A. Wallraff, Digital quantum simulation of spin models with circuit quantum electrodynamics, Phys. Rev. X **5**, 021027 (2015).

[14] C. S. Wang, J. C. Curtis, B. J. Lester, Y. Zhang, Y. Y. Gao, J. Freeze, V. S. Batista, P. H. Vaccaro, I. L. Chuang, L. Frunzio, L. Jiang, S. M. Girvin, and R. J. Schoelkopf, Efficient multiphoton sampling of molecular vibronic spectra on a superconducting bosonic processor, Phys. Rev. X **10**, 021060 (2020).

[15] A. H. Karamlou, W. A. Simon, A. Katabarwa, T. L. Scholten, B. Peropadre, and Y. Cao, Analyzing the performance of variational quantum factoring on a superconducting quantum processor, npj Quantum Inf. **7**, 156 (2021).

[16] C. Neill, T. McCourt, X. Mi, Z. Jiang, M. Y. Niu, W. Mruczkiewicz, I. Aleiner, F. Arute, K. Arya, J. Atalaya, R. Babbush, J. C. Bardin, R. Barends, A. Bengtsson, A. Bourassa, M. Broughton, B. B. Buckley, D. A. Buell, B. Burkett, N. Bushnell *et al.*, Accurately computing the electronic properties of a quantum ring, Nature (London) **594**, 508 (2021).

[17] J. Han, W. Cai, L. Hu, X. Mu, Y. Ma, Y. Xu, W. Wang, H. Wang, Y. P. Song, C.-L. Zou, and L. Sun, Experimental simulation of open quantum system dynamics via Trotterization, Phys. Rev. Lett. **127**, 020504 (2021).

[18] J. Braumüller, A. H. Karamlou, Y. Yanay, B. Kannan, D. Kim, M. Kjaergaard, A. Melville, B. M. Niedzielski, Y. Sung, A. Vepsäläinen, R. Winik, J. L. Yoder, T. P. Orlando, S. Gustavsson, C. Tahan, and W. D. Oliver, Probing quantum information propagation with out-of-time-ordered correlators, Nat. Phys. **18**, 172 (2022).

[19] X. Zhang, W. Jiang, J. Deng, K. Wang, J. Chen, P. Zhang, W. Ren, H. Dong, S. Xu, Y. Gao, F. Jin, X. Zhu, Q. Guo, H. Li, C. Song, A. V. Gorshkov, T. Iadecola, F. Liu, Z.-X. Gong, Z. Wang *et al.*, Digital quantum simulation of floquet symmetry-protected topological phases, Nature (London) **607**, 468 (2022).

[20] Y.-H. Shi, Y. Liu, Y.-R. Zhang, Z. Xiang, K. Huang, T. Liu, Y.-Y. Wang, J.-C. Zhang, C.-L. Deng, G.-H. Liang, Z.-Y. Mei, H. Li, T.-M. Li, W.-G. Ma, H.-T. Liu, C.-T. Chen, T. Liu, Y. Tian, X. Song, S. P. Zhao *et al.*, Observing topological zero modes on a 41-qubit superconducting processor, Phys. Rev. Lett. **131**, 080401 (2023).

[21] P. Roushan, C. Neill, J. Tangpanitanon, V. M. Bastidas, A. Megrant, R. Barends, Y. Chen, Z. Chen, B. Chiaro, A. Dunsworth, A. Fowler, B. Foxen, M. Giustina, E. Jeffrey, J. Kelly, E. Lucero, J. Mutus, M. Neeley, C. Quintana, D. Sank *et al.*, Spectroscopic signatures of localization with interacting photons in superconducting qubits, Science **358**, 1175 (2017).

[22] S. McArdle, S. Endo, A. Aspuru-Guzik, S. C. Benjamin, and X. Yuan, Quantum computational chemistry, Rev. Mod. Phys. **92**, 015003 (2020).

[23] A. Peruzzo, J. McClean, P. Shadbolt, M.-H. Yung, X.-Q. Zhou, P. J. Love, A. Aspuru-Guzik, and J. L. O'Brien, A variational eigenvalue solver on a photonic quantum processor, Nat. Commun. **5**, 4213 (2014).

[24] F. Arute, K. Arya, R. Babbush, D. Bacon, J. C. Bardin, R. Barends, S. Boixo, M. Broughton, B. B. Buckley, D. A. Buell, B. Burkett, N. Bushnell, Y. Chen, Z. Chen, B. Chiaro, R. Collins, W. Courtney, S. Demura, A. Dunsworth, E. Farhi *et al.*, Hartree-fock on a superconducting qubit quantum computer, Science **369**, 1084 (2020).

[25] P. J. J. O'Malley, R. Babbush, I. D. Kivlichan, J. Romero, J. R. McClean, R. Barends, J. Kelly, P. Roushan, A. Tranter, N. Ding, B. Campbell, Y. Chen, Z. Chen, B. Chiaro, A. Dunsworth, A. G. Fowler, E. Jeffrey, E. Lucero, A. Megrant, J. Y. Mutus *et al.*, Scalable quantum simulation of molecular energies, Phys. Rev. X **6**, 031007 (2016).

[26] A. Kandala, A. Mezzacapo, K. Temme, M. Takita, M. Brink, J. M. Chow, and J. M. Gambetta, Hardware-efficient variational quantum eigensolver for small molecules and quantum magnets, Nature (London) **549**, 242 (2017).

[27] C. Hempel, C. Maier, J. Romero, J. McClean, T. Monz, H. Shen, P. Jurcevic, B. P. Lanyon, P. Love, R. Babbush, A. Aspuru-Guzik, R. Blatt, and C. F. Roos, Quantum chemistry calculations on a trapped-ion quantum simulator, Phys. Rev. X **8**, 031022 (2018).

[28] J. I. Colless, V. V. Ramasesh, D. Dahlen, M. S. Blok, M. E. Kimchi-Schwartz, J. R. McClean, J. Carter, W. A. de Jong, and I. Siddiqi, Computation of molecular spectra on a quantum processor with an error-resilient algorithm, Phys. Rev. X **8**, 011021 (2018).

[29] Y. Nam, J.-S. Chen, N. C. Pisenti, K. Wright, C. Delaney, D. Maslov, K. R. Brown, S. Allen, J. M. Amini, J. Apisdorf, K. M. Beck, A. Blinov, V. Chaplin, M. Chmielewski, C. Collins, S. Debnath, K. M. Hudek, A. M. Ducore, M. Keesan, S. M. Kreikemeier *et al.*, Ground-state energy estimation of the water molecule on a trapped-ion quantum computer, npj Quantum Inf. **6**, 33 (2020).

[30] C. Kokail, C. Maier, R. van Bijnen, T. Brydges, M. K. Joshi, P. Jurcevic, C. A. Muschik, P. Silvi, R. Blatt, C. F. Roos, and P. Zoller, Self-verifying variational quantum simulation of lattice models, Nature (London) **569**, 355 (2019).

[31] R. Sagastizabal, S. P. Premaratne, B. A. Klaver, M. A. Rol, V. Negîrneac, M. S. Moreira, X. Zou, S. Johri, N. Muthusubramanian, M. Beekman, C. Zachariadis, V. P. Ostroukh, N. Haider, A. Bruno, A. Y. Matsuura, and L. DiCarlo, Variational preparation of finite-temperature states on a quantum computer, npj Quantum Inf. **7**, 130 (2021).

[32] J. Tilly, G. Jones, H. Chen, L. Wossnig, and E. Grant, Computation of molecular excited states on ibm quantum computers using a discriminative variational quantum eigensolver, Phys. Rev. A **102**, 062425 (2020).

[33] S. Gocho, H. Nakamura, S. Kanno, Q. Gao, T. Kobayashi, T. Inagaki, and M. Hatanaka, Excited state calculations using variational quantum eigensolver with spin-restricted ansätze and automatically-adjusted constraints, npj Comput. Mater. **9**, 13 (2023).

[34] R. Santagati, J. Wang, A. A. Gentile, S. Paesani, N. Wiebe, J. R. McClean, S. Morley-Short, P. J. Shadbolt, D. Bonneau, J. W. Silverstone, D. P. Tew, X. Zhou, J. L. O'Brien, and M. G. Thompson, Witnessing eigenstates for quantum simulation of hamiltonian spectra, Sci. Adv. **4**, eaap9646 (2018).

[35] K. Yeter-Aydeniz, B. T. Gard, J. Jakowski, S. Majumder, G. S. Barron, G. Siopsis, T. S. Humble, and R. C. Pooser, Benchmarking quantum chemistry computations with variational, imaginary time evolution, and krylov space solver algorithms, Adv. Quantum Technol. **4**, 2100012 (2021).

[36] G. S. Barron, B. T. Gard, O. J. Altman, N. J. Mayhall, E. Barnes, and S. E. Economou, Preserving symmetries for variational quantum eigensolvers in the presence of noise, Phys. Rev. Appl. **16**, 034003 (2021).

[37] J. J. Meyer, M. Mularski, E. Gil-Fuster, A. A. Mele, F. Arzani, A. Wilms, and J. Eisert, Exploiting symmetry in variational quantum machine learning, PRX Quantum **4**, 010328 (2023).

[38] C. Lyu, X. Xu, M.-H. Yung, and A. Bayat, Symmetry enhanced variational quantum spin eigensolver, Quantum **7**, 899 (2023).

[39] S. Bravyi, A. Kliesch, R. Koenig, and E. Tang, Obstacles to variational quantum optimization from symmetry protection, Phys. Rev. Lett. **125**, 260505 (2020).

[40] B. T. Gard, L. Zhu, G. S. Barron, N. J. Mayhall, S. E. Economou, and E. Barnes, Efficient symmetry-preserving state preparation circuits for the variational quantum eigensolver algorithm, npj Quantum Inf. **6**, 10 (2020).

[41] K. M. Nakanishi, K. Mitarai, and K. Fujii, Subspace-search variational quantum eigensolver for excited states, Phys. Rev. Res. **1**, 033062 (2019).

[42] W. Qian, R. Basili, S. Pal, G. Luecke, and J. P. Vary, Solving hadron structures using the basis light-front quantization approach on quantum computers, Phys. Rev. Res. **4**, 043193 (2022).

[43] C. Lyu, X. Tang, J. Li, X. Xu, M.-H. Yung, and A. Bayat, Variational quantum simulation of long-range interacting systems, New J. Phys. **25**, 053022 (2023).

[44] O. Higgott, D. Wang, and S. Brierley, Variational Quantum Computation of Excited States, Quantum **3**, 156 (2019).

[45] L. Mineh and A. Montanaro, Accelerating the variational quantum eigensolver using parallelism, Quantum Sci. Technol. **8**, 035012 (2023).

[46] C.-L. Hong, L. Colmenarez, L. Ding, C. L. Benavides-Riveros, and C. Schilling, Quantum parallelized variational quantum eigensolvers for excited states, arXiv:2306.11844.

[47] S. Endo, S. C. Benjamin, and Y. Li, Practical quantum error mitigation for near-future applications, Phys. Rev. X **8**, 031027 (2018).

[48] A. Kandala, K. Temme, A. D. Córcoles, A. Mezzacapo, J. M. Chow, and J. M. Gambetta, Error mitigation extends the computational reach of a noisy quantum processor, Nature (London) **567**, 491 (2019).

[49] Y. Kim, C. J. Wood, T. J. Yoder, S. T. Merkel, J. M. Gambetta, K. Temme, and A. Kandala, Scalable error mitigation for noisy quantum circuits produces competitive expectation values, Nat. Phys. **19**, 752 (2023).

[50] J. Chu, X. He, Y. Zhou, J. Yuan, L. Zhang, Q. Guo, Y. Hai, Z. Han, C.-K. Hu, W. Huang, H. Jia, D. Jiao, S. Li, Y. Liu, Z. Ni, L. Nie, X. Pan, J. Qiu, W. Wei, W. Nuerbolati *et al.*, Scalable algorithm simplification using quantum and logic, Nat. Phys. **19**, 126 (2023).

[51] Y. Xu, J. Chu, J. Yuan, J. Qiu, Y. Zhou, L. Zhang, X. Tan, Y. Yu, S. Liu, J. Li, F. Yan, and D. Yu, High-fidelity, high-scalability two-qubit gate scheme for superconducting qubits, Phys. Rev. Lett. **125**, 240503 (2020).

[52] M. A. Rol, F. Battistel, F. K. Malinowski, C. C. Bultink, B. M. Tarasinski, R. Vollmer, N. Haider, N. Muthusubramanian,

A. Bruno, B. M. Terhal, and L. DiCarlo, Fast, high-fidelity conditional-phase gate exploiting leakage interference in weakly anharmonic superconducting qubits, Phys. Rev. Lett. **123**, 120502 (2019).

[53] D. C. McKay, C. J. Wood, S. Sheldon, J. M. Chow, and J. M. Gambetta, Efficient *z* gates for quantum computing, Phys. Rev. A **96**, 022330 (2017).

[54] A. Hashim, R. K. Naik, A. Morvan, J.-L. Ville, B. Mitchell, J. M. Kreikebaum, M. Davis, E. Smith, C. Iancu, K. P. O'Brien, I. Hincks, J. J. Wallman, J. Emerson, and I. Siddiqi, Randomized compiling for scalable quantum computing on a noisy superconducting quantum processor, Phys. Rev. X **11**, 041039 (2021).

[55] T. Koffel, M. Lewenstein, and L. Tagliacozzo, Entanglement entropy for the long-range ising chain in a transverse field, Phys. Rev. Lett. **109**, 267203 (2012).

[56] W. Nuerbolati, Z. Han, J. Chu, Y. Zhou, X. Tan, Y. Yu, S. Liu, and F. Yan, Canceling microwave crosstalk with fixed-frequency qubits, Appl. Phys. Lett. **120**, 174001 (2022).

[57] S. S. Elder, C. S. Wang, P. Reinhold, C. T. Hann, K. S. Chou, B. J. Lester, S. Rosenblum, L. Frunzio, L. Jiang, and R. J. Schoelkopf, High-fidelity measurement of qubits encoded in multilevel superconducting circuits, Phys. Rev. X **10**, 011001 (2020).